Nonlinear Dynamics and Vortex Mechanics for Energy Harvesting from Fluttering Wings

by

Dilip Thakur

A thesis presented to Lakehead University in fulfilment of the

thesis requirement for the degree of

Master of Science in Mechanical Engineering

Dr Muhammad Saif Ullah Khalid, Supervisor

Thunder Bay, Ontario, Canada, 2025

I hereby declare that I am the sole author of this thesis.

Dilip Thakur

I authorize Lakehead University to lend this thesis to other institutions or individuals for the purpose of scholarly research.

Dilip Thakur

I further authorize Lakehead University to reproduce this thesis by photocopying or by other means, in total or in part, at the request of other institutions or individuals for the purpose of scholarly research.

Dilip Thakur

Lakehead University requires the signatures of all persons using or photocopying this thesis.

Please sign below and give address and date.

Abstract

This research investigates the nonlinear aeroelastic dynamics and energy harvesting performance of a two-degrees-of-freedom NACA 0012 wing under varying reduced velocities and electrical load resistances. In the first part of this work related to two-dimensional computational simulations, nonlinear oscillations emerge near the critical reduced velocity $U^*_r = 6$, with large amplitude limit-cycle oscillations forming around $U^*_r = 8$ in the absence of an electrical loading. As the electrical resistance increases, this transition is delayed, indicating the damping effect of the energy extraction mechanism. Fourier spectral analysis reveals the presence of both odd and even superharmonics in the aerodynamic lift force, highlighting the strong nonlinear fluid-structure coupling, which becomes less prominent at higher resistances. Phase portraits and Poincare maps demonstrate clear transitions between periodic and chaotic states, particularly under low resistance conditions. The voltage output is strongly correlated with fluctuations in the lift force, reaching a maximum at intermediate resistance before declining due to nonlinear suppression. Flow visualizations uncover a range of vortex shedding patterns, including single, paired, and multi-pair vortex configurations that weaken at high resistances and lower U^*_r. Building upon the insights gained from two-dimensional simulations, this study is extended to three-dimensional configurations by systematically increasing the wing's spanwise length to 0.3c, 0.6c, and 0.9c. The three-dimensional analysis focuses on the conditions that yielded optimal voltage output in the two-dimensional simulation results, particularly at $U^*_r = 10$ for different load resistances. The objective is to examine how variations in spanwise length influence fluid-structure interactions, alter vortex formation and organization, and impact the onset and intensity of nonlinear behaviors. Also, the comparative analysis of the 3D and 2D results highlight

the influence of spanwise flow instabilities on the energy harvesting performance. These findings provide valuable insights for identifying optimal spanwise length and operational parameters that enhance power generation efficiency in flutter-based energy harvesting systems.

Acknowledgements

I would like to express my sincere gratitude to my supervisor, **Dr. Muhammad Saif Ullah Khalid**, for his exceptional guidance, continuous support, and insightful mentorship throughout the course of my research. His expertise, patience, and encouragement have been invaluable to both the development of this work and my growth as a researcher. It has been a privilege to work under his supervision.

I am also deeply thankful to my thesis committee members, **Dr. Ahmed Elshaer** and **Dr. Kefu Liu**, for their time, thoughtful feedback, and constructive suggestions, which have significantly enhanced the quality and clarity of this research.

I am deeply grateful to my colleagues and peers **Faisal Muhammad, Amirhossein Fardi, Maham Kamran, Hao Wang, Dev Nayak, and Zahra Maleksabet** whose support and friendship made my transition into graduate studies both smooth and rewarding.

Finally, I gratefully acknowledge the financial and computational support provided by the **Natural Sciences and Engineering Research Council of Canada (NSERC)**, the **Digital Research Alliance of Canada**, and **Lakehead University**. Their generous support and resources are instrumental in the successful completion of this research.

Contents

List of Figures

List of Tables

Chapter 1: Introduction

With the rising global demand for sustainable energy, researchers are increasingly exploring innovative technologies that can efficiently harvest and convert ambient energy into electricity. One promising area involves aeroelastic energy harvesters that rely on the dynamic behavior of fluttering airfoils. Unlike traditional rigid systems, these mechanisms take advantage of fluid-induced oscillations to produce continuous power. By embedding piezoelectric materials within the structure, the mechanical vibrations generated by flutter can be directly converted into electrical energy, making these systems well suited for a range of low-power applications. Over the past decade, numerous studies have worked to optimize the design and operation of such harvesters by investigating various structural configurations and flow conditions to improve their performance and energy efficiency [1], [2], [3], [4]. These investigations have collectively advanced our understanding of the underlying physics and improved the energy conversion efficiency of flapping foil-based harvesters, emphasizing their potential as a viable alternative to conventional wind and hydroelectric turbines. In contrast to traditional wind turbines that rely on rotational motion, flutter-based harvesters harness the self-sustained oscillations of airfoils interacting with fluid flow. This method offers several distinct advantages, such as the ability to operate in low velocity environments, scalability across different sizes, and improved power density [5], [6], [7].

Energy harvesting using passively flapping airfoils often associated with the phenomenon of flutter is fundamentally driven by the principles of fluid-structure interaction (FSI). Flutter is a type of dynamic aeroelastic instability that occurs in flexible structures, such as aircraft wings or

turbine blades, when aerodynamic forces interact with the structure's natural modes, resulting in self-sustained oscillations. These oscillations can increase in amplitude over time, potentially leading to either steady periodic motion or structural failure. In energy harvesting applications, this dynamic coupling allows for the continuous extraction of energy from the fluid flow by converting the airfoil's oscillatory motion into electrical power [8], [9], [10].

This fluid-structure coupling leads to the development of limit cycle oscillations (LCOs), which enable the continuous extraction of energy from the surrounding fluid flow. These oscillatory motions have been extensively investigated in terms of mechanical efficiency, with particular attention given to critical design parameters such as airfoil geometry [11], [12], mass ratio, moment of inertia, and the location of the pitching axis [13]. The pitching and heaving kinematics play a significant role in determining the overall energy conversion efficiency, as they are closely linked to the vortex dynamics that develop around the airfoil. In addition, the energy harvesting performance is strongly influenced by the Reynolds number and the reduced velocity [11], [13], [14]. Several studies have also reported notable variations in the energy harvesting capability of fluttering foils, underscoring the importance of fluid dynamic effects in optimizing their aeroelastic response [15]. Different types of electromechanical transducers have been integrated into flutter-based energy harvesting systems to enable the direct conversion of mechanical vibrations into electrical energy. These transducers include piezoelectric [16], [17], [18], [19] piezoresistive [20], electromagnetic, and electrostatic mechanisms [21], all of which support sustainable micro-power generation. The growing interest in micro-power generators (MPGs) has also been driven by progress in micro-machining technologies and the development of low-power electronic devices [13], [22][23].

A key factor in the performance of flutter-based energy harvesters lies in the inherent nonlinear dynamics that govern their behavior. Unlike conventional systems that depend on structural nonlinearities to trigger oscillations, recent studies have shown that fluid-induced nonlinearities alone can be sufficient to drive effective energy harvesting [24]. In systems with linear structural characteristics, nonlinear effects stemming from unsteady aerodynamic forces, vortex shedding, and wake interactions play a critical role in determining the amplitude, frequency, and stability of oscillations [25]. These fluid originated nonlinearities give rise to complex dynamic phenomena such as bifurcations, limit cycle oscillations (LCOs), and chaotic behavior, all of which significantly affect the efficiency and reliability of the energy harvesting process [26], [27], [28]. Moreover, the mechanical efficiency of these systems is highly sensitive to both structural parameters and flow conditions, making their optimization a critical focus of ongoing research [2], [29].

Despite significant progress in aeroelastic energy harvesting, most prior studies have primarily focused on systems with inherent structural nonlinearities, often neglecting the critical influence of nonlinear fluid dynamics. To address this gap, the present work investigates how fluid-induced nonlinearities arising solely from unsteady flow phenomena affect the energy harvesting performance of fluttering airfoils. A strongly coupled electro-aeroelastic model is developed to study the dynamics of a structurally linear system, where all observed nonlinearities stem from fluid-structure interactions.

The 2D computational analysis of this study systematically explores how these fluid-driven nonlinearities and vortex mechanics influence output power, stability, and bifurcation behavior as a function of reduced velocity. Particular attention is given to the onset of

nonlinearity, which can trigger dynamic stall and alter the nature of limit-cycle oscillations. The emergence of subharmonic and superharmonic frequency components is analyzed to gain insights into symmetry or asymmetric behavior, vortex shedding, and the resulting large-amplitude motions phenomena that play a crucial role in determining energy harvesting efficiency.

Building upon these 2D results, the study extends into three dimensions to examine how changes in spanwise length further influence system behavior. By analyzing results with varying span lengths (0.3c, 0.6c, 0.9c), the 3D investigation explains how spanwise flow structures and three-dimensional wake dynamics affect the harvesting performance. This extension enables a more realistic assessment of airfoil-based harvesters operating in unsteady low-speed flows.

The combined 2D and 3D analysis not only provides a deeper understanding of fluid-induced nonlinearities in flutter-based systems but also offers practical insights into optimizing design parameters for enhanced voltage output and system reliability. The findings contribute to filling a key gap in literature and enable the way for more effective deployment of energy harvesting technologies in real-world, unsteady aerodynamic environments.

Research Objectives:

The following are the primary objectives of this research:

- How do nonlinear dynamics and vortex mechanics influence energy harvesting from fluttering wings?
- How do nonlinear dynamics and vortex phenomena affect energy harvesting with variations in the span of the wings?

Chapter 2: Numerical Methodology

To model the coupled dynamics between fluid flow and elastically mounted structures, we adopt the Arbitrary Lagrangian Eulerian (ALE) formulation [13], [30]. In this framework, the conservation equations for mass and momentum, applicable to incompressible flows, are given as follows.

$$\frac{\partial u_j}{\partial x_j} = 0$$

$$\frac{\partial u_i}{\partial t} + u_j \frac{\partial u_i}{\partial x_j} = -\frac{1}{\rho}\frac{\partial p}{\partial x_i} + \frac{1}{Re}\frac{\partial^2 u_i}{\partial x_j \partial x_j}$$

Here $u_i = (u, v)$ are the Cartesian components of the fluid velocity, and p is the pressure. The indices $(i, j) = (1,2)$ represent the two Cartesian directions, where (x_i) refers to a specific coordinate direction, and (x_j) denotes the general spatial coordinates. The variable (p) indicates the fluid pressure, and (ρ) is the fluid density.

The Reynolds number is defined as:

$$Re = \frac{\rho c U_\infty}{\mu}$$

where 'c' is the chord length of the NACA-0012 airfoil, U_∞ is the free-stream velocity, and 'μ' is the dynamic viscosity of the fluid.

In the expression below, $\tilde{u}_j = (\tilde{u}, \tilde{v})$ represents the fluid velocity relative to the moving computational grid, where u_{gj} corresponds to the velocity of the grid itself. This relative velocity is defined as:

$$\tilde{u}_j = \left(u_j - u_{gj}\right)$$

To accurately resolve the boundary layer behavior, a non-staggered, body-fitted O-type grid is employed. The grid extends up to 20 chord lengths (20c) from the airfoil surface to ensure sufficient spatial resolution. In this mesh layout, all primary variables including velocity components and pressure are stored at the centers of the computational cells, while the fluxes are computed at the midpoints of the cell faces. Within the ALE framework, the computational mesh surrounding a moving structure adapts dynamically to follow the motion of the body. This flexible meshing approach allows the interior grid points to move arbitrarily, enabling the grid to adjust its shape and configuration while preserving overall mesh quality during deformation. Such adaptability is especially important in simulations involving large amplitude oscillations of rigid or flexible structures, where considerable mesh distortion would otherwise compromise solution accuracy. To ensure robust grid deformation, a re-meshing algorithm is integrated with the flow solver. In the present study, we employ the method proposed by[31], which utilizes the Radial Basis Function (RBF) interpolation technique. This approach effectively transmits boundary displacements throughout the computational domain, maintaining mesh integrity and preventing element inversion, even under significant structural motion.

The Radial Basis Function (RBF) interpolation $f(x_j)$ used to map the displacements of boundary nodes on the structural surface is mathematically expressed as:

$$f(x_j) = \sum_{i=1}^{N} \alpha_i \emptyset(\|x_j - x_i\|) + p_1(x_j),$$

In this formulation, $p_1(x_j)$ denotes a first-degree polynomial, and α_i are the coefficients associated with the basis functions. The RBF interpolation approach effectively transfers structural boundary displacements throughout the entire computational domain, enabling smooth and continuous mesh deformation while preserving the geometric integrity of the grid cells.

The interpolation relies on a set of control points strategically placed along the structure's boundary, with the total number of control points denoted by N_C. The radial basis function $\emptyset(\|\cdot\|)$ is evaluated using the Euclidean norm. In the present study, we employ the globally supported Thin Plate Spline (TPS) RBF, which is mathematically defined as:

$$\emptyset(x) = x^2 \log(x)$$

Also, $p_1(x_j)$ represents the following condition:

$$\sum_{i=1}^{N_c} \alpha_i p_1\left(x_{cj}(i)\right) = 0$$

The coefficients are obtained by enforcing that the interpolation function $f(x_j)$ exactly matches the prescribed displacements at the designated control points, as described by the following expression:

$$f(x_{cj}) = \Delta x_{cj}$$

Here, Δx_{cj} denotes the prescribed displacement at each control point x_{cj} . The selection of control points is carried out using a greedy algorithm, as outlined in [32]. Once the interpolation function is constructed, the displacements of all interior mesh nodes are evaluated

accordingly. In the subsequent step, the velocity of each grid node is computed by dividing its displacement by the discrete time step Δt. Thus, the velocity of a node located at x_j is given by:

$$u_{gj} = \frac{f(x_j)}{\Delta t}$$

The computed grid velocities are subsequently used to evaluate the relative flux terms $(\tilde{U} \text{and } \tilde{V})$ required by the flow solver. A key challenge associated with the RBF-based remeshing technique lies in its computational expense, as it involves solving a dense linear system whose size scales with the number of control points N_C. As this number increases, the resulting system becomes progressively ill-conditioned, making iterative solvers unsuitable for efficient solutions.

To address this, a direct linear solver specifically Gaussian elimination with partial pivoting is employed to factorize the coefficient matrix during the preprocessing phase. For enhanced computational performance, an explicit form of the RBF method is used in conjunction with the greedy algorithm to precompute the coefficient matrix. This precomputation significantly reduces the runtime overhead. At each time step, the unknowns within the interpolation scheme are resolved using successive forward and backward substitutions, thereby improving the overall efficiency and stability of the simulation process. Although computationally demanding, the RBF method offers excellent mesh quality preservation during large translational and rotational motions, outperforming conventional re-meshing strategies such as those proposed in [33]. Our implementation is fully parallelized and capable of supporting three-dimensional simulations involving bodies of infinite span.

However, first 2D simulations are conducted at low Reynolds numbers to suppress spanwise flow instabilities, ensuring flow remains effectively two-dimensional. The investigation of various design parameters provides critical insights into the structural response and wake

behavior of oscillating systems, which are essential for the development of efficient fluid-based energy harvesting technologies.

We employ the fractional-step method to solve the governing equations for fluid flow. In this method, the momentum equations are initially solved separately for each velocity component, temporarily disregarding the continuity constraint. During this prediction step, the pressure-gradient terms are either neglected or treated as known values, leading to the calculation of an intermediate velocity field, denoted by [33].

To enforce incompressibility, a pressure Poisson equation is then solved, derived from the divergence-free condition of the velocity field. The resulting pressure field is used to correct the intermediate velocities, ensuring that the final velocity field satisfies the incompressibility constraint.

For spatial discretization, finite difference schemes are applied. Central differencing is used for all spatial derivatives except for the convective terms, which are handled using the Quadratic Upwind Interpolation for Convective Kinematics (QUICK) scheme [34]. This scheme adopts a directionally biased stencil, selecting the upwind-biased interpolation based on the direction of the local flux expressed as:

$$\widetilde{U}_j = \frac{\left(\widetilde{U}_j + \left|\widetilde{U}_j\right|\right)}{2}, \qquad \widetilde{U}^-_j = \frac{\left(\widetilde{U}_j - \left|\widetilde{U}_j\right|\right)}{2}$$

The temporal term is discretized using a semi-implicit scheme. Specifically, the diagonal diffusion terms are treated using the implicit Crank–Nicolson method, chosen for its favorable stability properties, while the remaining terms are advanced in time using the two-step explicit Adams-Bashforth method. For a comprehensive discussion of the discretization techniques, boundary conditions, and the parallelization approach, readers are referred to [30], [35], [36].

The resulting linear system is efficiently solved using the line successive over-relaxation (SOR) method, which is particularly well-suited for structured grid arrangements. The numerical scheme's stability is governed by the Courant Friedrichs Lewy (CFL) condition, which dictates that the maximum CFL number within the domain must remain below one. The local CFL number is defined as:

$$\mathrm{CFL} = \left(\frac{|\mathrm{u}|}{\Delta \mathrm{x}} + \frac{|\mathrm{v}|}{\Delta \mathrm{y}}\right) = \Delta \mathrm{t} \mathrm{J}^{-1}(|\widetilde{\mathrm{U}}| + |\widetilde{\mathrm{V}}|)$$

where u and v are the components of flow velocity in the x and y directions, respectively, and J denotes the Jacobian.

A. Flow domain and geometry

1. 2D Flow domain and geometry:

In the two-dimensional flow analysis, an O-grid is employed, which is particularly for resolving the flow around bodies with circular or airfoil-like geometries. In this case, the grid is constructed around a NACA 0012 airfoil, whose chord length is normalized to unity. The airfoil is surrounded by concentric grid layers, forming an O-shaped structured mesh that ensures a smooth and continuous distribution of grid points around the surface. This configuration allows for grid refinement in the near-body region, where flow gradients are typically high, thereby capturing boundary layer effects and wake development with greater accuracy. The grid spacing increases gradually away from the airfoil, reducing computational cost while maintaining fidelity. The outer boundary of the domain is set at a distance of 20 times the chord length (20c) from the airfoil, which ensures that far-field boundary conditions do not interfere with the near-field flow

dynamics around the airfoil and the following boundary conditions used are mentioned in Table 1.

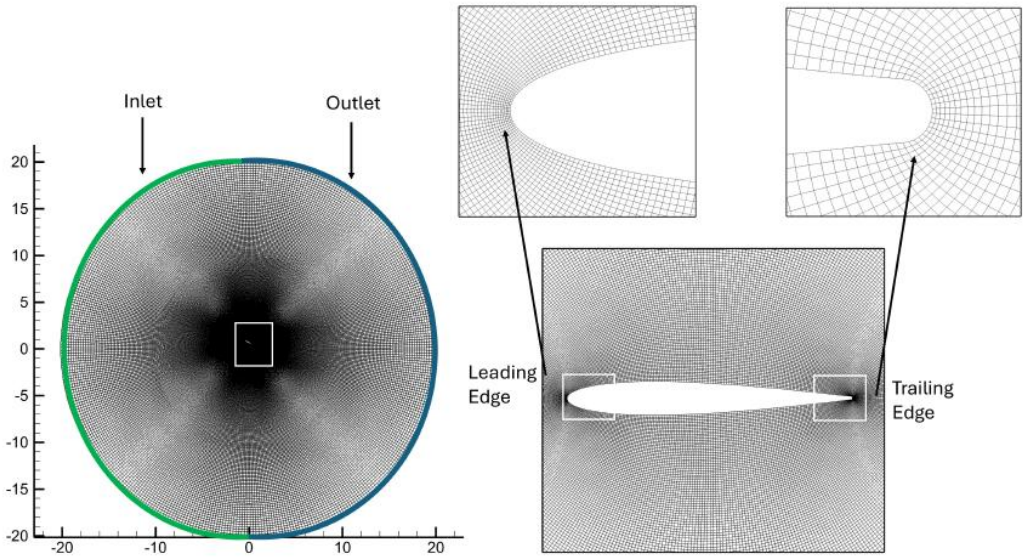

Figure 1: O-type body-fitted grid around an NACA-0012 airfoil

Table 1: 2D domain boundary conditions

Boundary	**Condition Type**	**Mathematical Expression**	**Description**
Inlet	Dirichlet	$u_x = U_\infty, v_y = 0$	Uniform inflow with free-stream velocity
Outlet	Neumann	$\frac{\partial u}{\partial x} = 0,\ \frac{\partial v}{\partial x} = 0,$ $\frac{\partial p}{\partial x} = 0$	Zero-gradient (outflow)

Surface of the foil	No-slip Wall	$u_x = 0, v_y = 0$	Fluid sticks to surface (no slip or penetration)
Top & Bottom	Free-slip Wall	$v_y = 0, \quad \frac{\partial u}{\partial y} = 0$	No normal flow

2. 3D Flow domain and geometry:

For the 3D simulations, the 2D O-grid is extended into the spanwise direction to generate a fully structured 3D mesh. The baseline 2D grid, constructed around the NACA 0012 airfoil with a chord length normalized to unity, is extruded along the z-axis to specified spanwise lengths of 0.3c, 0.6c and 0.9c. The corresponding spanwise discretization's employ 24, 48, and 72 uniformly spaced nodes, respectively. This extrusion preserves fine near-body resolution in both the chordwise and normal directions essential for accurately capturing boundary-layer development and near-wake dynamics, while introducing the necessary spanwise extent to resolve three-dimensional flow phenomena such as spanwise flow and wake instabilities. The grid spacing in the spanwise direction is kept uniform to maintain numerical stability, and the mesh is designed to preserve cell orthogonality and smoothness across all three dimensions, thereby minimizing interpolation errors.

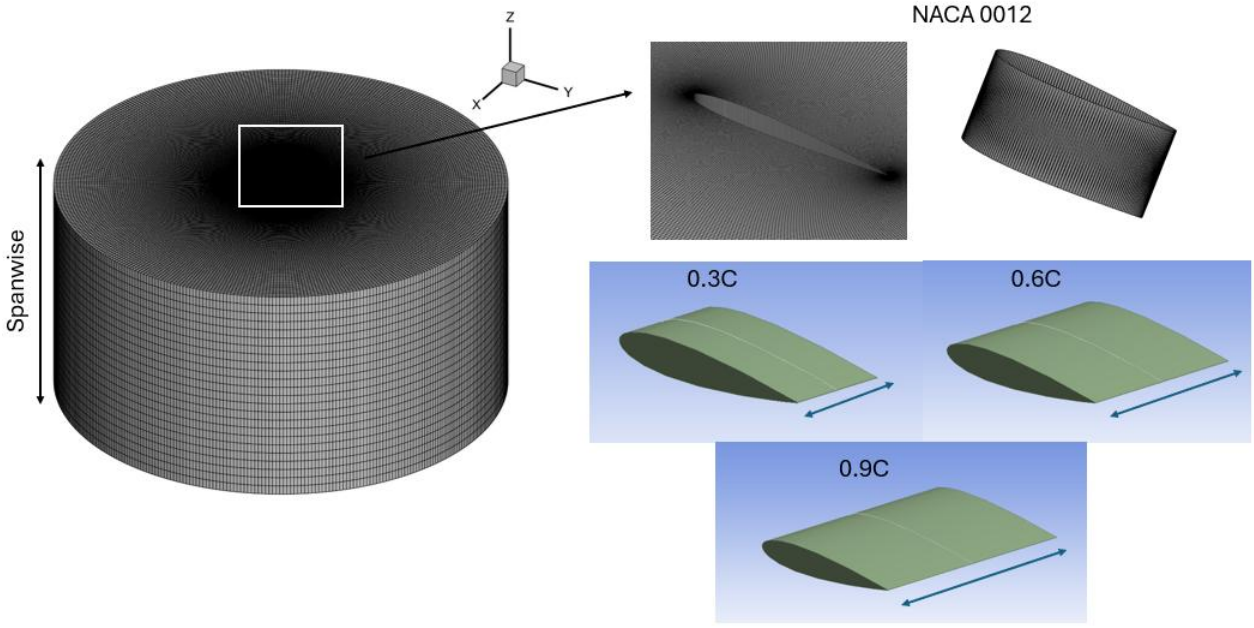

Figure 2: 3D Mesh configurations and different lengths of airfoil in the spanwise direction

B. Aerodynamic forces and moments acting on the airfoil

The interaction between a fluid and a solid body immersed within it gives rise to forces primarily resulting from pressure and shear stress distributions acting on the body's surface. The aerodynamic behavior of such systems is commonly characterized using three fundamental non-dimensional parameters: the lift coefficient C_L, the drag coefficient C_D, and the moment coefficient C_D. These coefficients are defined mathematically as follows:

$$C_L = \frac{F_y(t)}{\frac{1}{2}\rho U_\infty^2 c}, \qquad C_D = \frac{F_x(t)}{\frac{1}{2}\rho U_\infty^2 c}, \qquad C_M = \frac{M_\theta(t)}{\frac{1}{2}\rho U_\infty^2 c^2}$$

Here, $F_x(t)$ and $F_y(t)$ denote the instantaneous drag and lift forces acting on the structure, respectively, while $M_\theta(t)$ represents the moment about the rotational axis located at x_p, which corresponds to the position of the elastic supports. The chord length of the foil, denoted by 'c', serves as the characteristic length scale of the structure. These non-dimensional

coefficients provide critical insight into the aerodynamic performance and dynamic response of systems subjected to fluid-structure interactions.

C. Electromechanical model

The electromechanical coupling in the energy harvesting system, as depicted in Figure 3, is primarily driven by the structural motion of the airfoil, which induces electrical power generation through piezoelectric transducers. The governing equations of this coupled aeroelastic system are formulated in a non-dimensional framework to capture the dynamic interaction between structural displacement and the resulting electrical response. In particular, the non-dimensional plunging displacement is described by eq. (1) and eq. (2)**,** as referenced in [30], [37].

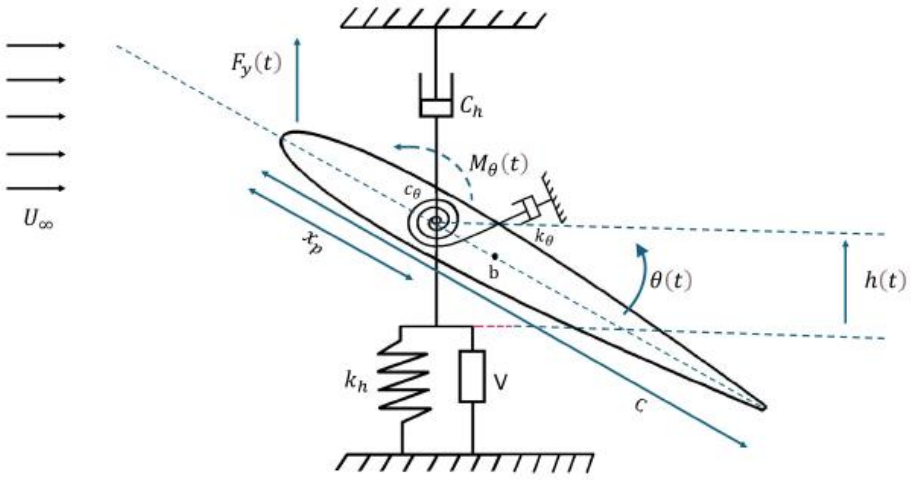

Figure 3: Schematic diagram of an airfoil-based piezo aeroelastic energy harvester

$$\ddot{h}^* + 2\zeta_h\left(\frac{2\pi}{U_r^*}\right)\dot{h}^* + \left(\frac{2\pi}{U_r^*}\right)^2 h^* - S^*\left(cos\theta\cdot\ddot{\theta} \;\; - sin\theta\cdot\dot{\theta}^2\right) - \left(\frac{1}{U_r^*}\right)^2 V^* = \frac{2\cdot C_L}{\pi m^*} \qquad (1)$$

$$\ddot{\theta} + 2\zeta_\theta\bar{f}\left(\frac{2\pi}{U_r^*}\right)\dot{\theta} + \left(\bar{f}\frac{2\pi}{U_r^*}\right)^2\theta - \frac{S^*}{r_\theta^2}cos\theta\cdot\ddot{h} = \frac{2\cdot C_M}{\pi r_\theta^2 m^*} \qquad (2)$$

$$\dot{V}^* + \sigma_1\cdot\dot{h}^* + \frac{\sigma_2}{U_r^*}\cdot V^* = 0 \qquad (3)$$

The non-dimensional heaving displacement is defined as $\mathrm{h}^* = \frac{\mathrm{h}}{\mathrm{c}}$, where 'h' denotes the heaving displacement and 'c' is the chord length of the airfoil, which is set to unity for simplification. The pitching motion is represented by the angular displacement 'θ', and reduced velocity is defined as $\mathrm{U}_\mathrm{r}^* = \frac{\mathrm{U}_\infty}{\mathrm{f_n}\cdot \mathrm{c}}$. The radius of gyration, characterizing the mass distribution of the airfoil about its axis of rotation, is given by $\mathrm{r}_\theta = \sqrt{\frac{\mathrm{I}_\theta}{\mathrm{m_h L}^2}}$, where I_θ is the moment of inertia, $\mathrm{m_h}$ is the structural mass, and 'L' is a characteristic length scale. The ratio of natural frequencies is defined as $\bar{\mathrm{f}} = \frac{\mathrm{f}_\theta}{\mathrm{f_h}}$, where $\mathrm{f_h and}\ \mathrm{f}_\theta$ are the heaving and pitching frequencies, respectively. In this study, the heaving and pitching frequencies are chosen such that $\bar{\mathrm{f}} = 1$, ensuring that the heaving and pitching motions are synchronized, since both frequencies are same therefore, we represented by '$\mathrm{f_n}$' called as natural structural frequency.

The linear spring constants satisfy the constraint as $\frac{\mathrm{k}_\theta}{\mathrm{k_h}} = \frac{\mathrm{m_h}}{\mathrm{I}_\theta}$ outlined in [14][38]. Finally, the static imbalance defined as the ratio of the distance between the elastic axis and the center of mass to the chord length is expressed as $\mathrm{S}^* = \frac{\mathrm{b}}{\mathrm{C}}$, and is fixed at a value of -0.04 throughout this work.

The structural frequency of the airfoil in the heaving direction is given by $f_h = \frac{1}{2\pi}\sqrt{\frac{k_h}{m_h}}$, where k_h is the linear structural stiffness, and m_h is the mass per unit length of the airfoil. For pitching motion, the frequency is defined by $f_\theta = \frac{1}{2\pi}\sqrt{\frac{k_\theta}{I_\theta}}$.

The system's linear structural damping ratio associated with the heaving degree of freedom is expressed as $\zeta_h = \frac{c_h}{2(\sqrt{k_h m_h})}$, and mass ratio is defined as $m^* = \frac{m_h}{m_f}$, where $m_f = \frac{\rho\pi c^2}{4}$, represents the mass of the fluid displaced and $m^* = 10$.

By incorporating piezoelectric coupling introduces additional non-dimensional parameters. The non-dimensional voltage is defined as $V^* = \frac{V}{V_o}$, where 'V' is the generated voltage, and V_o is the reference voltage given by $V_o = \frac{m_h f_h^2 L}{\theta_L}$. Also, the electromechanical coupling coefficient θ_L, valued is $1.55 * \frac{10^{-3}N}{V}$. Two additional non-dimensional parameters, σ_1 and σ_2, are used to characterize the piezoelectric behavior. These are defined as $\sigma_1 = \frac{\theta_L^2}{m_h C_p f_h^2}$ and $\sigma_2 = \frac{1}{RC_p f_h}$, where C_P is the capacitance, measured in nanofarad, which is $120\ nF$, and R is the load resistance measure in $k\Omega$[39]. The governing first-order ordinary differential equation for voltage contains three key terms: one representing the rate of voltage change, another indicating the strength of piezoelectric coupling, and a third capturing energy dissipation through the electrical circuit. Additionally, I_θ denotes the mass moment of inertia, and the radius of gyration 'r' is defined as 0.548c from the axis of rotation.

D. Verification

1. 2D Verification of grid independence

To establish mesh independence, simulations are performed using three structured grid resolutions: 196 × 256 (coarse), 304 × 400 (medium), and 464 × 600 (fine). The computational model involves a NACA 0012 airfoil subjected to combined pitching and heaving motions at a Reynolds number of $\mathrm{Re} = 1100$. The reduced velocity is defined as $\mathrm{U^*r} = \frac{\mathrm{U_\infty}}{\mathrm{f_n \cdot c}}$, where the free-stream velocity ($\mathrm{U_\infty}$) is set to 1, and $'\mathrm{f_n}'$ is the natural structural frequency.

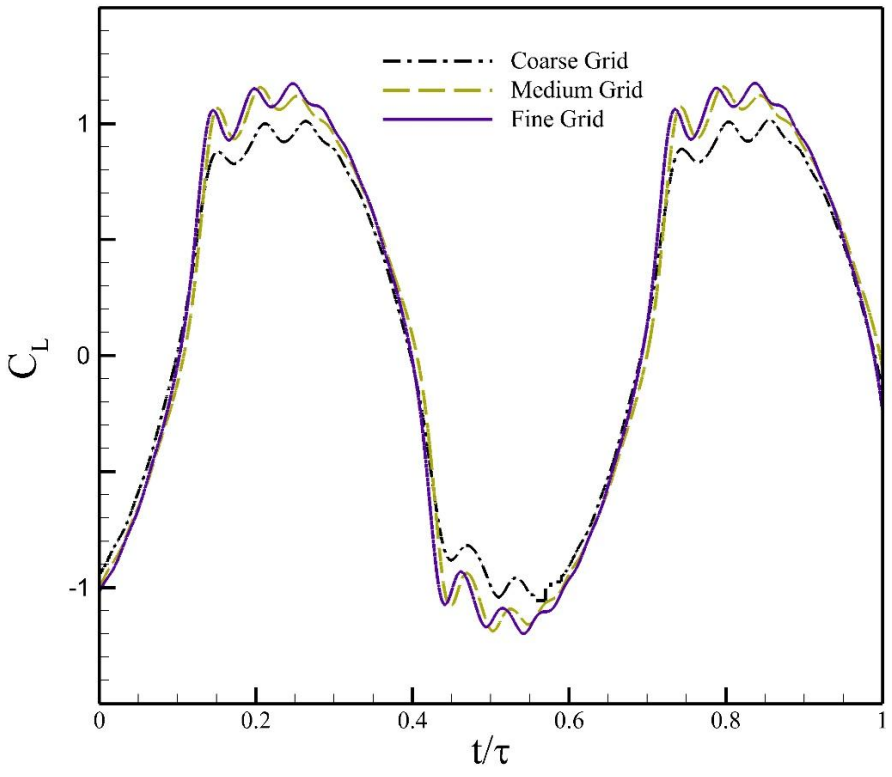

Figure 4: Result for the grid-independence study

The unsteady aerodynamic response is characterized by the lift coefficient (C_L) over non-dimensional time. As depicted in Figure 4, the medium and fine grids produce nearly overlapping C_L profiles, indicating negligible variation with further grid refinement. To quantify the level of convergence, root-mean-square (RMS) values of C_L are computed at statistically steady conditions, yielding values of 0.800165, 0.878834, and 0.884199 for the coarse, medium, and fine grids, respectively (refer to Table 2). The relative error in RMS C_L between the coarse and medium grids is approximately 9.52%, while the difference between the medium and fine grids is only 0.61%.

Table 2: Grid resolution and corresponding RMS values of C_L

Grid	$\mathbf{N_x}$	$\mathbf{N_y}$	**Size**	$\mathbf{C_L\ (RMS)}$	**Relative error (%)**
G1	196	256	50176	0.800165	G1 and G2 (9.52%)
G2	**304**	**400**	**121600**	**0.878834**	G2 and G3 (**0.61%**)
G3	464	600	278400	0.884199	

Based on these observations, the medium grid is selected for all subsequent simulations, offering an optimal compromise between computational efficiency and numerical accuracy.

2. 2D Verification of timestep independence

For time step independence, additional simulations are conducted using the medium grid resolution. The results of this time-step sensitivity analysis are presented in Figure 5. Three

different time-step sizes are tested, corresponding to 5000, 8000, and 10,000 discrete steps per oscillation cycle of the airfoil. The oscillation period $'\tau'$ was selected based on the reference study by Farooq et al.[13]. All flow conditions remained consistent with those used in the previously described grid-independence analysis.

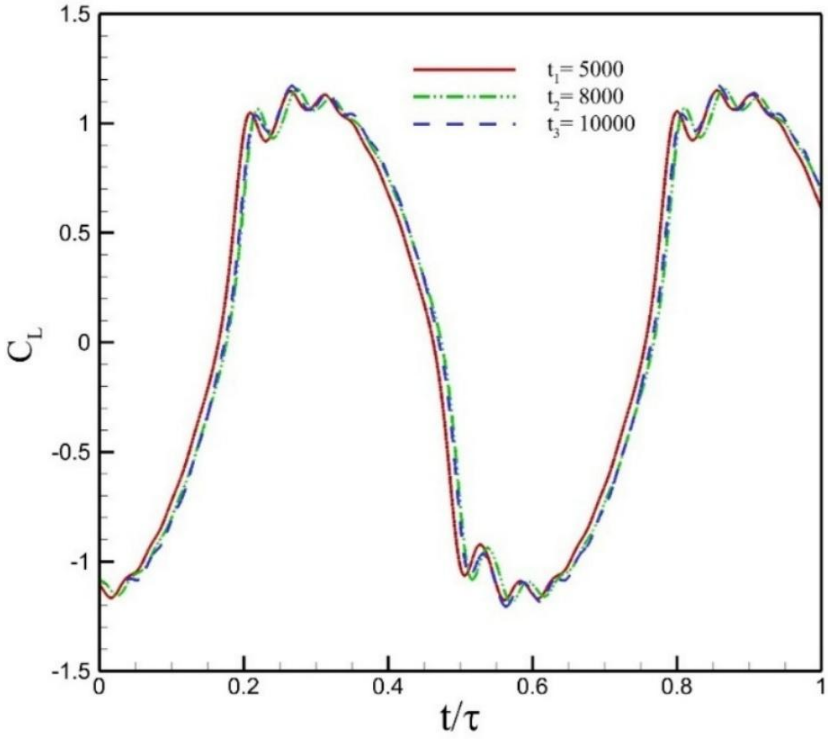

Figure 5: Results for the time-step convergence study

The root-mean-square (RMS) values of the lift coefficient (C_L) for the three cases are found to be 0.890442, 0.892498, and 0.894194, respectively, as summarized in Table 3. The relative error between the 5000 and 8000 steps simulation cases was approximately 0.4196%, while the difference between the 8000 and 10,000 steps cases further decreased to 0.1897%. These results demonstrate that the solution becomes progressively insensitive to further

reductions in the time-step size, indicating temporal convergence. It is worth noting that 8000-time steps per cycle correspond to a time-step size of $\Delta t = 0.000125$ sec.

Table 3: Convergence study for different time-steps

Time steps	Grid	$C_L(RMS)$	Relative error (%)
5000	Medium	0.890422	T1 and T2 (9.52%)
8000		0.892498	
1000		0.894194	T2 and T3 (**0.61%**)

Additional validation of the numerical results obtained using the in-house solver can be found in Refs. [30], [35], [40] .

3. 3D Verification of grid independence

For the 3D simulations, the medium-resolution grid from the 2D configuration (304 × 400) is adopted as the base mesh and extruded into the spanwise direction. Three spanwise lengths are considered to investigate the influence by 3D. To maintain a consistent spatial resolution across all cases, the grid spacing in the spanwise direction is kept constant. This is achieved by defining spanwise spacing as $x = \frac{L}{N_Z}$, where L is the spanwise length which is 0.3c, 0.6c and 0.9c and N_Z is the number of nodes along the z-axis. Accordingly, N_Z is set to 24, 48, and 72 for spanwise lengths of 0.3c, 0.6c and 0.9c respectively, thereby ensuring uniform cell dimensions throughout the computational domain and preserving numerical accuracy when comparing results across different spanwise configurations.

Table 4: 3D Domain size at different spanwise length

Grid	$\mathbf{N_x}$	$\mathbf{N_y}$	$\mathbf{N_z}$	**Spanwise length**	**Total number of nodes**
G2	304	400	24	0.3c	2,918,400
	304	400	48	0.6c	5,851,392
	304	400	72	0.9c	8,777,088

Chapter 3: Two-Dimensional Fluid-Structure-Electrical Interactions

We investigate the flow over a two-degree-of-freedom (2DoF) NACA 0012 airfoil at a Reynolds number of 1100, with translational and rotational damping ratios of $\zeta_h = 0.008$ and $\zeta_\theta = 0.050$, respectively, determined based on the mass ratio (m^*) and the moment of inertia (I_θ). The simulations are performed over a range of reduced velocities (U_r^*) from 1 to 12, which serves as the primary control parameter influencing both the effective damping and stiffness of the system. For each case, the root-mean-square (RMS) values of the non-dimensional heaving displacement (h^*), pitch angle(θ), lift coefficient (C_L), and drag coefficient (C_D) are computed and presented as functions of (U_r^*) for different values of the electrical resistance (R), as illustrated in Figure 6.

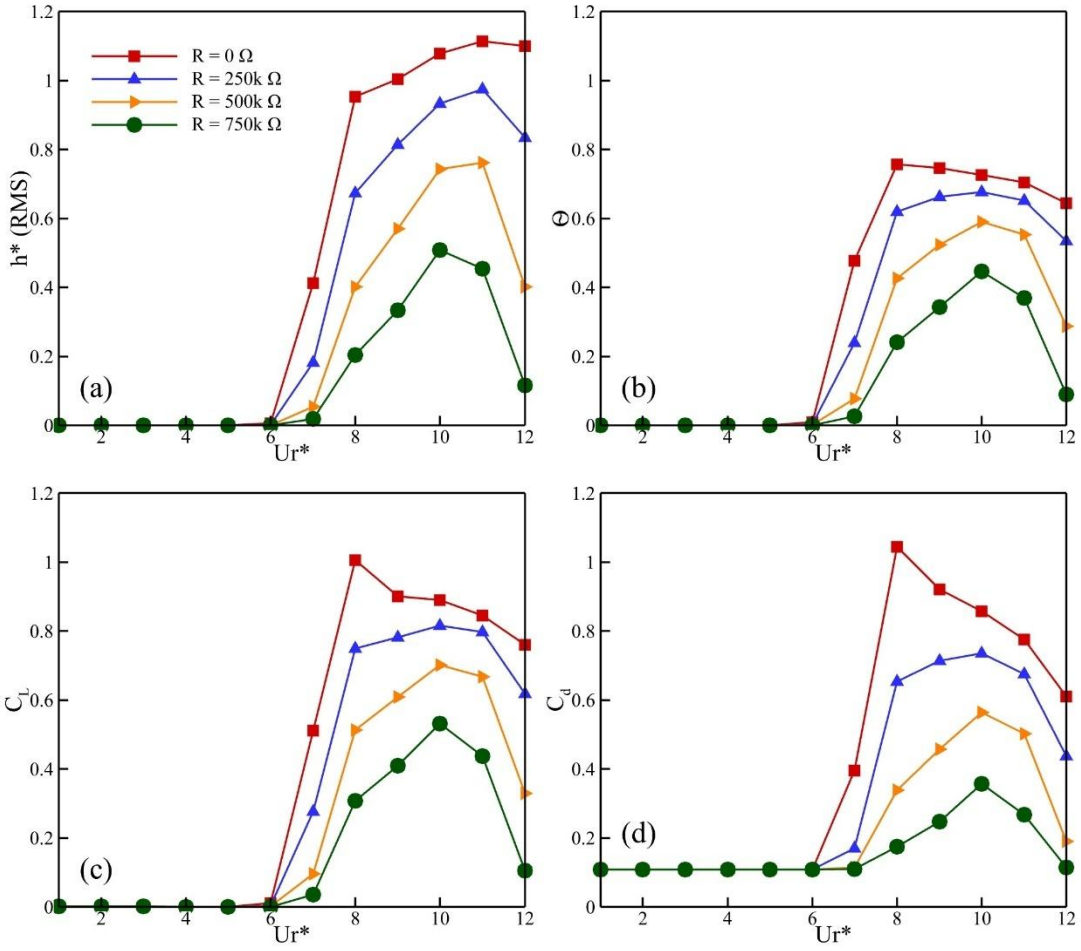

Figure 6: Dependence of (a) h*(RMS), (b) θ, (c) C_L, (d) C_D on U_r^* for R = 0, 250, 500, and 750 kΩ

From the plots, for $U_r^* \in [1,5]$, the airfoil remains in a stable state with no discernible oscillations, regardless of the electrical resistance. Around $U_r^* = 6$, small-amplitude motions appear, marking the onset of self-excited oscillations. As U_r^* increases to 7, these oscillations become sustained, with amplitudes continuing to grow until reaching a certain peak value. This overall trend is consistently observed in (h^*), (θ), (C_L), and (C_D).

In Figure 6a, which shows the evolution of (h^*), the amplitude begins to rise beyond U_r^* = 6, for $R = 0\ k\Omega$, reaching its maximum at $U_r^* = 11$. For $R > 0$, oscillations also initiate near

U_r^*=6, and the peak amplitude is reached at U_r^* = 11 for $R = 250 \text{ and } 750\ k\Omega$, but at U_r^* = 10 , $R = 0\ k\Omega$, the heaving amplitude shifted towards the lower reduced velocity.

In Figure 6b, the pitching amplitude attains its peak at U_r^* = 8 for the case of $R = 0\ k\Omega$, whereas the presence of electrical resistance $R > 0$ shifts this peak to U_r^* = 10. A comparable shift is evident in Figure 6c-d for the (C_L), and (C_D), respectively, with maxima occurring at U_r^* = 8 under zero resistance and at U_r^* = 10 when a resistive load is applied. Following these maxima, the amplitudes of (θ), (C_L), and (C_D), progressively decline, suggesting that load-induced damping begins to dominate, driving the system toward to lower oscillations.

Interestingly, the heaving amplitude in Figure 6a deviates from this general pattern for $R = 0$, exhibiting a delayed response before aligning with the decay trend observed in the other parameters. Across all cases, increasing resistance consistently suppresses oscillation amplitudes and shifts the bifurcation point to higher reduced velocities. Beyond U_r^* = 10, the damping effect introduced by the electrical load becomes the prevailing influence on the system's response, substantially attenuating the oscillations and returning to steady-state motion. To gain deeper insight into the system dynamics, we select the reduced velocity U_r^* corresponding to the highest observed C_L amplitude for each load resistance and analyze the temporal evolution of the lift coefficient through Temporal-history plots.

- **Temporal-history plots of C_L**

The temporal histories of the lift coefficient C_L after the system reaches steady-state dynamic response are presented in Figure 7. The lift coefficient serves as a fundamental parameter, directly representing the fluid–structure interaction dynamics and acting as a primary indicator of the vortex-shedding frequency. Therefore, its behavior is critical for assessing the

energy harvesting performance of the system. Figure 7a illustrates the C_L time history corresponding to U_r^* = 8 under $R = 0$. In this case, C_L exhibits large-amplitude, periodic limit-cycle oscillations with consistent peak-to-peak variations. The signal is characterized by asymmetry and irregularities, which signify the presence of nonlinear effects within the system. These temporal profiles provide important information on the initiation and progression of nonlinearities under different control parameters, influencing the overall dynamic response of the nonlinear aeroelastic energy harvesting system.

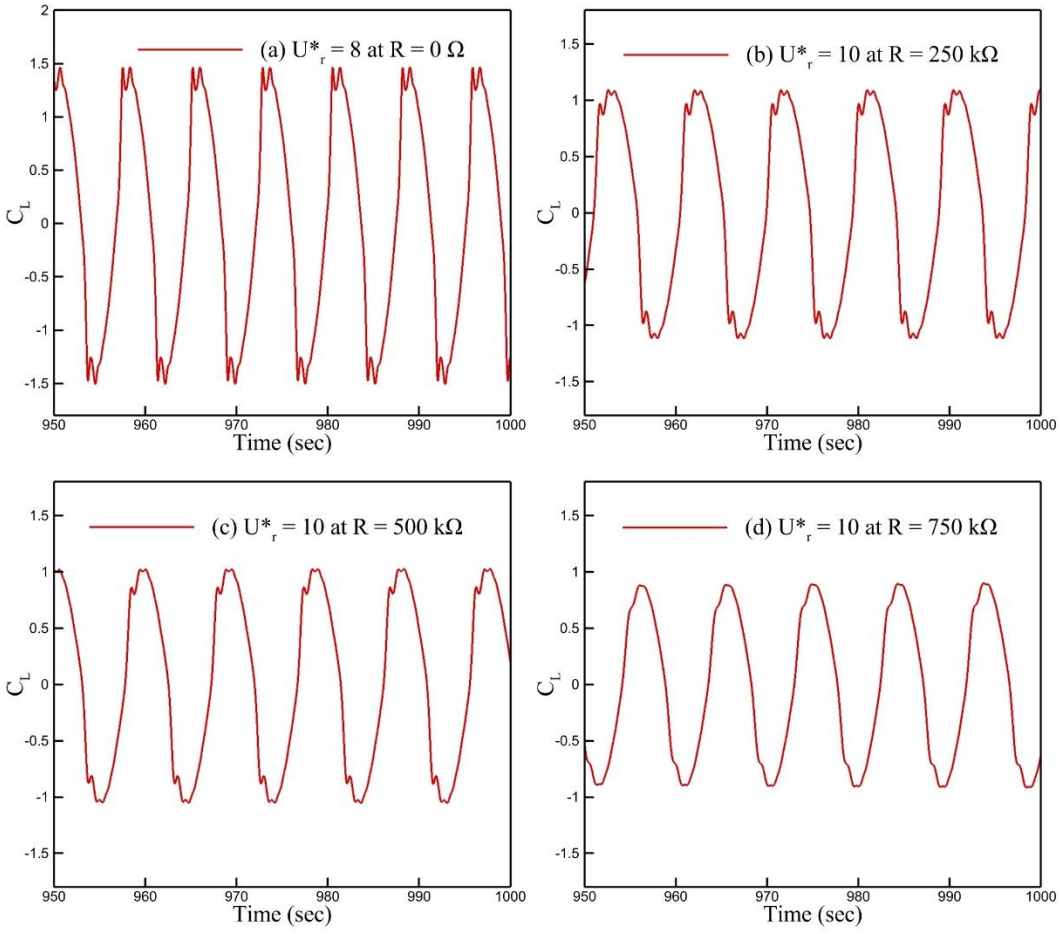

Figure 7: Temporal histories of C_L with the maximum amplitude at (a) U_r^* = 8 and R = 0 Ω, (b) U_r^* = 10 and R = 250 kΩ, (c) U_r^* = 10 and R = 500 kΩ, and (d) U_r^* = 10 and R = 750 kΩ

With an increase in load resistance to $\mathrm{R} = 250\ \mathrm{k\Omega}$, as shown in Figure 7b, the $\mathrm{C_L}$ becomes smoother and exhibits reduced distortion, accompanied by a significant decrease in amplitude. This behavior reflects enhanced damping introduced by the electrical load. A similar pattern is observed at $\mathrm{R} = 500\ \mathrm{k\Omega}$ in Figure 7c, where the signal further smooths and the amplitude decreases, indicating stronger damping effects. At $\mathrm{R} = 750\ \mathrm{k\Omega}$, depicted in Figure 7d, the signal shows minimal asymmetry and skewness, demonstrating substantial suppression of nonlinear dynamics. The increased load-induced damping reduces the lift coefficient and shifts the system toward a near quasi nonlinear state through energy extraction. These findings highlight the critical role of resistive aerodynamic damping in attenuating nonlinear behavior, as evidenced by the progressive changes in signal amplitude and shape. To further examine the nonlinear characteristics of the system, the frequency spectra of the lift and drag coefficients are evaluated using Fast Fourier Transform (FFT) analysis.

- **Fast Fourier-Transform plots**

An FFT-based analysis of $\mathrm{C_L}$ is performed for all cases across the full range of reduced velocities considered in this study. However, only the representative cases corresponding to the maximum $\mathrm{C_L}$ amplitude for FFT plots with some neighboring reduced velocities, to illustrate how the system's nonlinearity develops or decays.

Table 5: FFT analysis for selected U_r^*

FFT Analysis for Selected Reduced Velocities ($\mathbf{U_r^*}$)		
$\mathrm{R\ (k\Omega)}$	$\mathrm{U_r^*}$	Sub-figure
0	7-9	a-c
250	10-12	d-f

500	10-12	g-h
750	10-12	j-l

For $U_r^* \in$ [0,5], the oscillations are extremely small, approaching zero. At U_r^* = 6, a slight growth in oscillation is observed, although the amplitude remains limited. Consequently, the analysis focuses on cases at $R = 0$ for reduced velocities $U_r^* \in$ [7,9], capturing the onset and amplification of nonlinear behavior, as evidenced by the evolution of spectral peaks. $R > 0$, a similar pattern is observed in the range $U_r^* = [10 - 12]$, reflecting the transition from peak C_L amplitudes to reduced oscillation levels. This reduction is attributed to the increased damping introduced by the electrical load, which mitigates the nonlinear dynamics of the system.

At $R = 0$, as U_r^* increases from 7 to 12, the spectra exhibit multiple frequency components, indicating the onset and progression of nonlinear behavior and this multi-frequency response, including a broadband spectrum suggestive of chaotic dynamics, is observed for cases with non-zero low load resistance within the same U_r^* range. However, this complex response persists only up to a certain higher U_r^* value as the load resistance increases. The fundamental frequency remains the dominant component in the system's dynamic response, representing the primary vibration mode excited under the given conditions. This fundamental frequency closely approximates but does not exactly coincide with the structure's natural frequency, the inherent frequency at which it vibrates freely without external forcing or damping. This slight discrepancy, documented in Table 6. Notably, the dominant frequency is consistent across all resistance values considered ($R = 0,\ 250, 500, \text{and } 750\ \text{k}\Omega$), with corresponding frequency values also provided

in Table 6. It is important to highlight that at higher $\mathrm{U}_{\mathrm{r}}^{*}$ values, the fundamental frequency increasingly deviates from the natural structural frequency.

Table 6: Fundamental and natural structural frequencies for $R = 0 - 750\ k\Omega$ at various U_r^*

$\mathbf{U}_{\mathbf{r}}^{*}$	**Fundamental Frequency (Hz)**	**Natural Structural Frequency (Hz)**
6	0.1699	0.16666
7	0.14500	0.14285
8	0.1300	0.12500
9	0.11500	0.11111
10	0.10500	0.10000
11	0.09499	0.09090
12	0.08999	0.08333

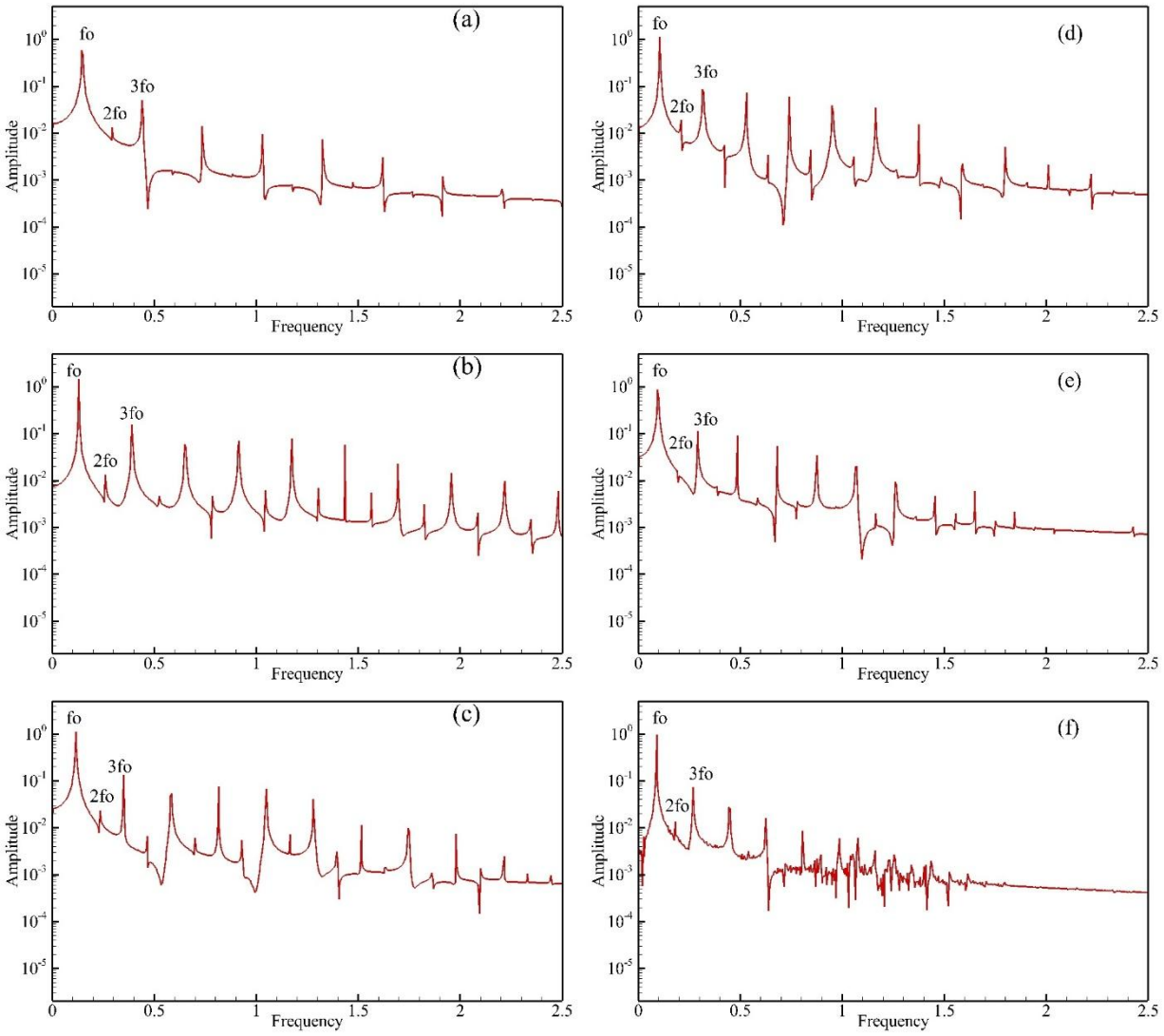

Figure 8: Spectra of C_L at $R = 0\ \Omega$: (a) U_r^* = 7, (b) U_r^* = 8, (c) U_r^* = 9; and at $R = 250\ k\Omega$, (d) U_r^* = 10, (e) $U^*{}_r$ = 11, (f) U_r^* = 12

The FFT spectra of C_L reveals prominent contributions from both odd and even harmonics of the fundamental frequency (f_o), indicating the presence of both cubic and quadratic nonlinearities within the system, as shown in Figures 8 and 9. None of the spectra display subharmonics, suggesting the absence of period-doubling phenomena and incommensurate

frequencies. The observed superharmonic peaks arise from nonlinear effects associated with quadratic and cubic terms in the system dynamics. Specifically, quadratic nonlinearities induce response asymmetry and redistribute energy across superharmonics at integer multiples of the fundamental frequency (i.e., $2f_o$ $3f_o$, etc.) [26]. Similar behavior is observed in the C_L spectra at higher U_r^*, as depicted in Figures 8 and 9**.**

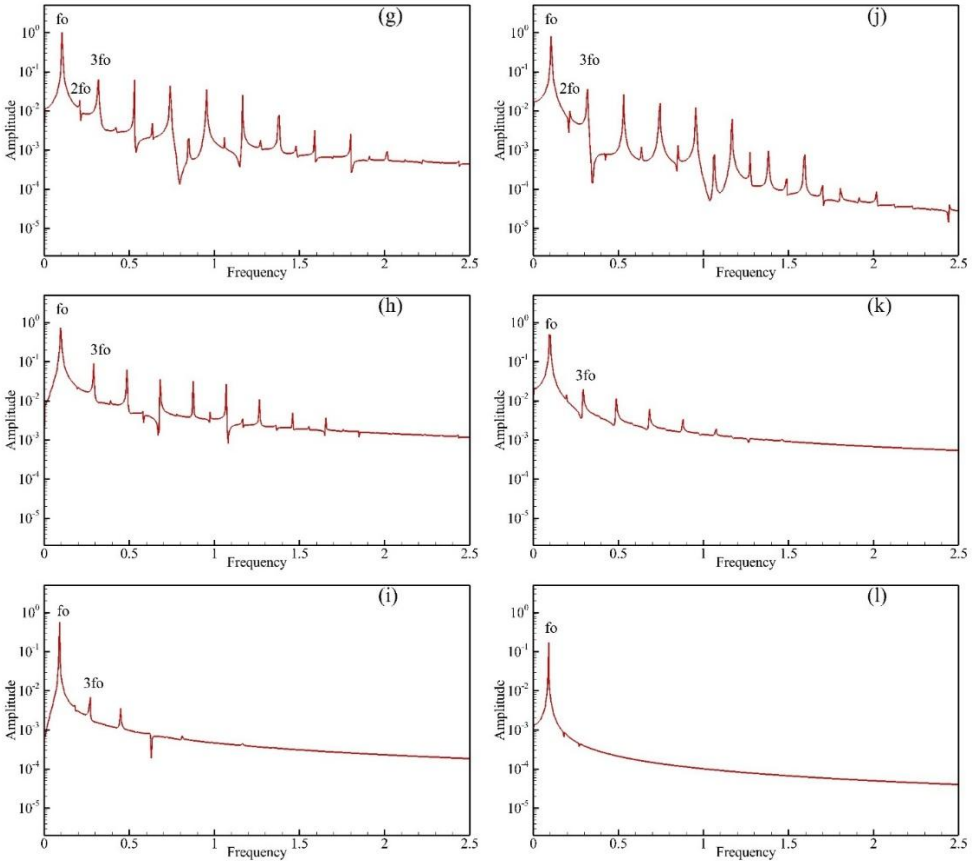

Figure 9: Spectra of C_L at $R = 500\ k\Omega$: (g–i) for U_r^* = 10–12, and at $R = 750\ k\Omega$: (j–l) for U_r^* = 10–12

The superharmonics and nonlinearities exhibit sensitivity to changes in load resistance. At $R = 0$, both odd and even harmonics are clearly present. As U_r^* and R increase and the

amplitudes of these harmonics gradually decrease. Within the C_L spectra, the harmonic amplitude decay follows a distinct pattern: even harmonics diminish first, followed by the odd harmonics. This asymmetric decay behavior in the frequency spectrum has been previously reported by Hammond et al. [38]. In the present study, this trend is evident in Figures 8a-8f and 9g-9l. At $U_r^* = 12$ and $R = 750\ k\Omega$, the FFT spectrum is dominated by a single fundamental frequency with very weak superharmonics and minimal spectral energy distributed across other frequencies. This indicates the system transitions toward quasi-nonlinear behavior, characterized by weak nonlinearity and low-amplitude oscillations in the lift coefficient C_L . This reduction in oscillation amplitude is also reflected in the corresponding temporal histories shown in Figure 7**.**

To further investigate the absence of subharmonics in the system's response, the FFT spectra of the drag coefficient C_D are presented in Figure 10. These spectra reveal the presence of superharmonics only, with the second harmonic (twice the fundamental frequency) being the most prominent. Even harmonics consistently exhibit higher amplitudes than odd harmonics, indicating that even harmonics contribute more substantially to the signal's energy and dominate the spectral content across varying load resistance values. Since the spectra does not show the emergence of additional frequencies as the control parameters increase, they provide limited insight into any potential transition to chaotic behavior in the system.

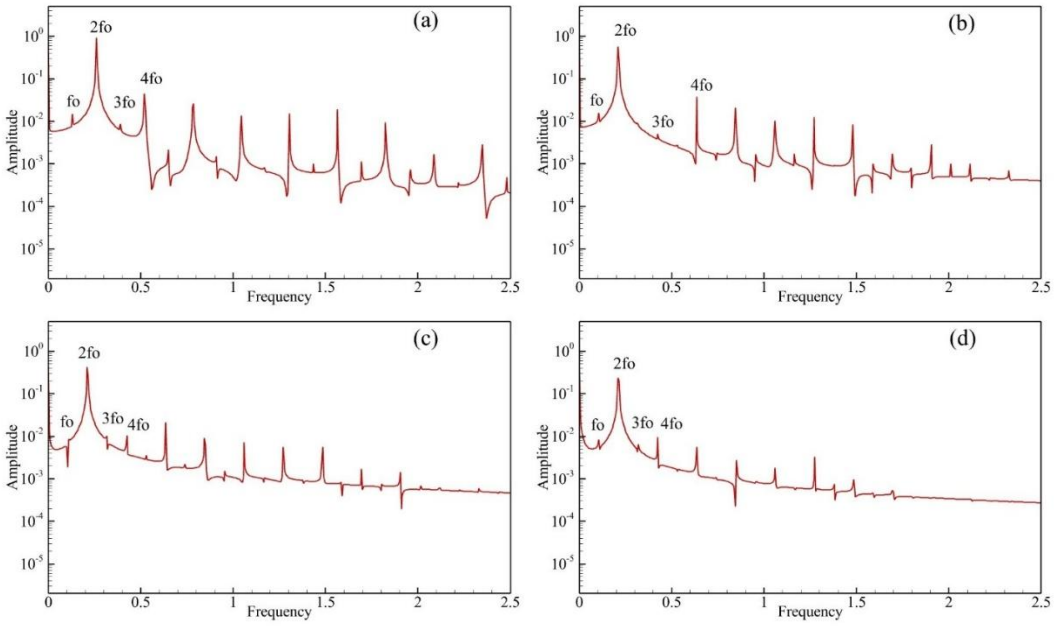

Figure 10: Spectra of C_D at (a) U_r^** = 8, $R = 0\ \Omega$; (b) U_r^* = 10, $R = 250\ k\Omega$; (c) U_r^* = 10, $R = 500\ k\Omega$; (d) U_r^* = 10, $R = 750\ k\Omega$

To overcome this limitation, phase portraits plotting C_L versus C_D are analyzed. These visualizations provide qualitative insights into the system's phase-space dynamics, revealing key features of its temporal evolution and offering a deeper understanding of the underlying nonlinearities.

- **Phase portraits**

Phase maps are constructed using C_L and C_D to investigate the system's temporal evolution by visualizing its trajectories, as illustrated in Figures 11 and 12**.** The phase portraits reveal increasing skewness, particularly along the C_D axis toward positive values, with the shape extending more prominently to the right compared to the left, where C_L increases up to $U_r^* = 8$. Beyond this point, the trajectories become narrower and less skewed as C_L decreases except for the case shown in Figure 11a, which exhibits quasi-nonlinear behavior on a very small scale.

Figure 11c displays the most pronounced asymmetry, indicating strong quadratic nonlinear interactions. With increasing load resistance, the skewness and distortion of the phase portraits gradually diminish, suggesting that enhanced electrical damping suppresses quadratic nonlinear effects. Additionally, phase portraits are examined across varying U_r^* values. At $R = 0\ k\Omega$ and $U_r^* = 6$, the airfoil undergoes low-amplitude oscillations dominated by a single frequency. The corresponding phase portrait in Figure 11a shows a thick, closed-loop trajectory with smooth progression, indicative of a near-periodic response governed by fluid-structure interactions.

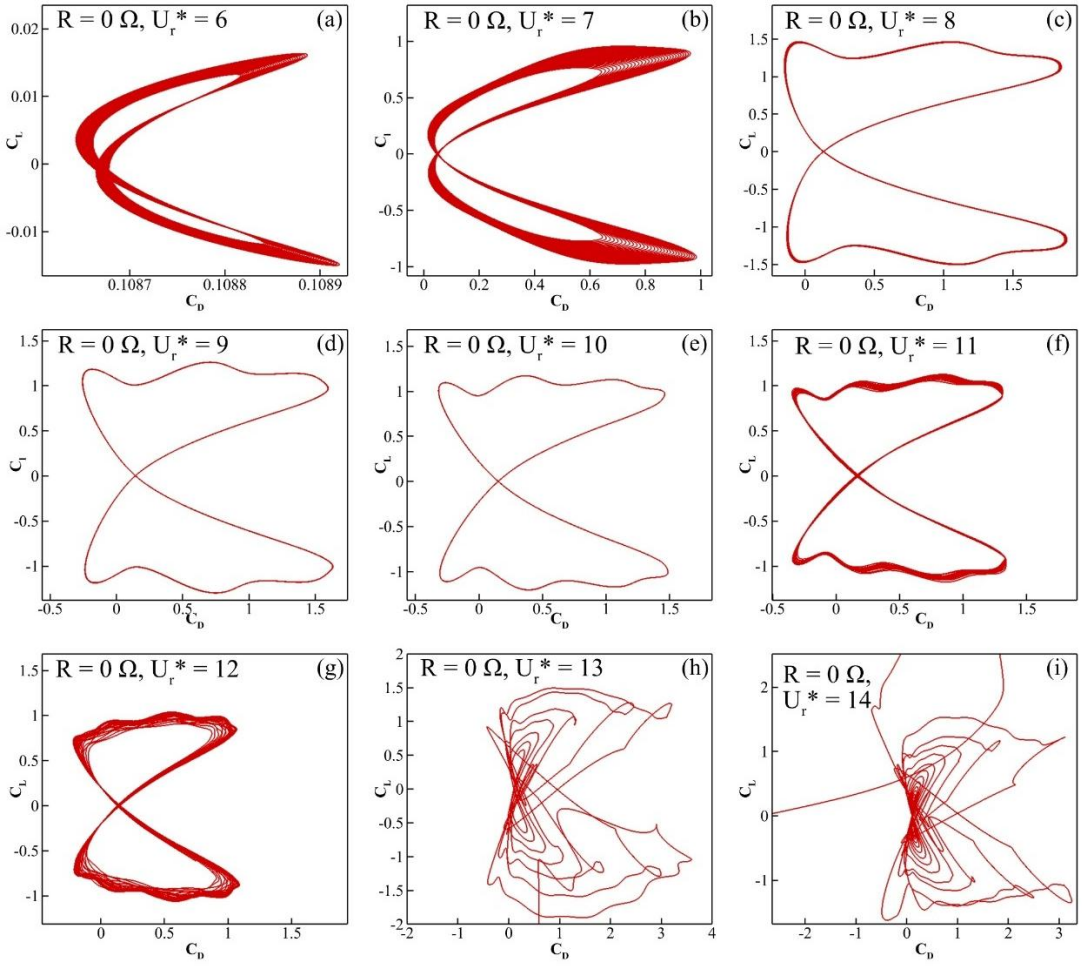

Figure 11: Phase portraits at $R = 0$. (a-b) Transition phase close to quasi-nonlinear. (c–g) Periodic state. (h-i) chaotic behavior, as indicated by irregular trajectories

As U_r^* increases to 7 and beyond, the amplitude of C_L steadily grows. At $U_r^* = 8$, the trajectory forms a thinner, well-defined closed loop, as shown in Figure 11c, indicating the establishment of a stable periodic limit-cycle oscillation (LCO) [17], [26], [41]. This double-looped pattern between C_D and C_L further suggests that C_D oscillates at twice the frequency of C_L. Specifically, a full loop appears for C_L, while only a half loop is observed for C_D, confirming that C_D varies at double the frequency of C_L, as depicted in Figure 11. The airfoil maintains high amplitudes of both C_L and C_D up to $U_r^* = 8$ in Figure 10c. As U_r^* increases toward 12, the phase portraits display increasingly irregular trajectories, characterized by distorted loops and irregularities, signaling a transition toward chaotic dynamics, as illustrated in Figures 11e-11g**.**

To investigate the system's behavior beyond this regime, a simulation was performed at a higher U_r^*. The resulting phase portraits, shown in Figures 11h-11i, exhibit non-uniform, open-loop trajectories characteristic of chaotic dynamics. In this state, both C_L and C_D increase more rapidly, indicating that aerodynamic forces dominate the structural response, with nonlinearities primarily arising from fluid dynamics rather than the structure itself.

When the electrical load resistance is introduced, the system's transition pathway is altered. Initially, the trajectory thickens, with both C_L and C_D increasing as U_r^* rises. Around $U_r^* = 10$, the system enters a limit-cycle oscillation (LCO) regime, characterized by maximum amplitudes and a broader, closed-loop trajectory, as shown in Figure 12. At higher U_r^* values and increased resistance, the oscillations become damped, and the airfoil's trajectory evolves into a smoother closed loop. However, the time required to reach the LCO state increases with increasing R and U_r^*, indicating enhanced damping and a shift toward quasi-nonlinear behavior,

as also illustrated in Figure 9**.** The corresponding FFT spectra shows dominant frequency peaks with very weak superharmonics, which is reflected in the very small, closed loop observed in Figure 12i. It is important to note that this response is not considered strictly linear due to the presence of these weak nonlinear components. This method offers qualitative insights into the system's behavior, enabling the distinction between periodic, quasiperiodic, and chaotic regimes based on the spatial patterns and distributions of points within the map. To gain deeper insight into the system's state, Poincare maps are plotted for further analysis.

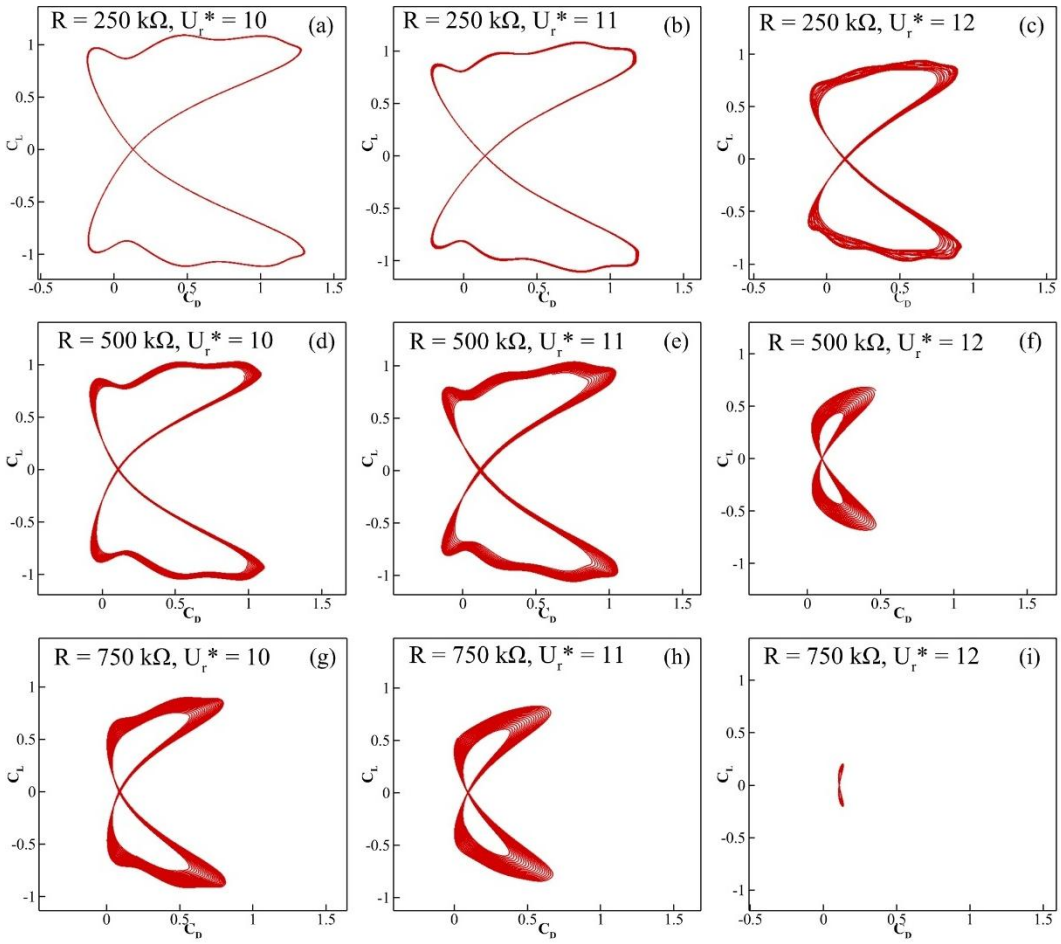

Figure 12: Phase portraits from U_r^* = 10 to 12. (a–c) $R = 250\ k\Omega$, (d–f) $R = 500\ k\Omega$, (g–i) $R = 750\ k\Omega$

The highest amplitude appears at lower U_r^*, and the system moves towards low amplitude as R increases, and the sequence progresses from left to right.

- **Poincare maps**

Poincare maps are generated for cases exhibiting higher $\mathrm{C_L}$ values across different load resistances. For $\mathrm{R} = 0\ \mathrm{k\Omega}$, maps are shown at $\mathrm{U_r^*}$ = 8 and 13. The Poincare sections are created by plotting $\mathrm{C_L}$ versus $\mathrm{C_D}$ at three characteristic points in the oscillation cycle corresponding to the maximum, zero, and minimum heaving amplitudes.

For $\mathrm{R} = 0\ \mathrm{k\Omega}$ at $\mathrm{U_r^*}$ = 8, Figures 13a–13c illustrate that the points initially appear widely dispersed but gradually converge or overlap over time. This behavior signifies a transition from quasi-nonlinear to periodic nonlinear dynamics, where the system repeatedly returns to the same point in the Poincare section, indicating a steady state with a consistent trajectory. This pattern is evident in Figures 13a–13c and persists for $\mathrm{U_r^*}$ values up to 12.

As $\mathrm{U_r^*}$ increases further, the Poincare points shown in Figures 13d-13f initially cluster but then disperse into scattered distributions. This pattern indicates a transition from a periodic limit-cycle oscillation (LCO) to chaotic dynamics via a crisis route, consistent with the distorted, open-loop trajectories observed in the phase portraits of Figures 11h-11i. The trajectory loses its periodicity, exhibiting irregular bursts as $\mathrm{U_r^*}$ surpasses a critical threshold. Corresponding FFT spectra shows no evidence of subharmonics, thereby ruling out period-doubling, period-n, or incommensurate frequencies associated with quasi-periodic states. The increase in $\mathrm{U_r^*}$ intensifies aerodynamic forcing on the structure, while simultaneously reducing effective damping and spring stiffness. These effects cause the system to follow a non-uniform trajectory that does not

revisit the same points in the Poincare section, further evidence of the onset of chaotic behavior as illustrated in Figures 11h-11i**.**

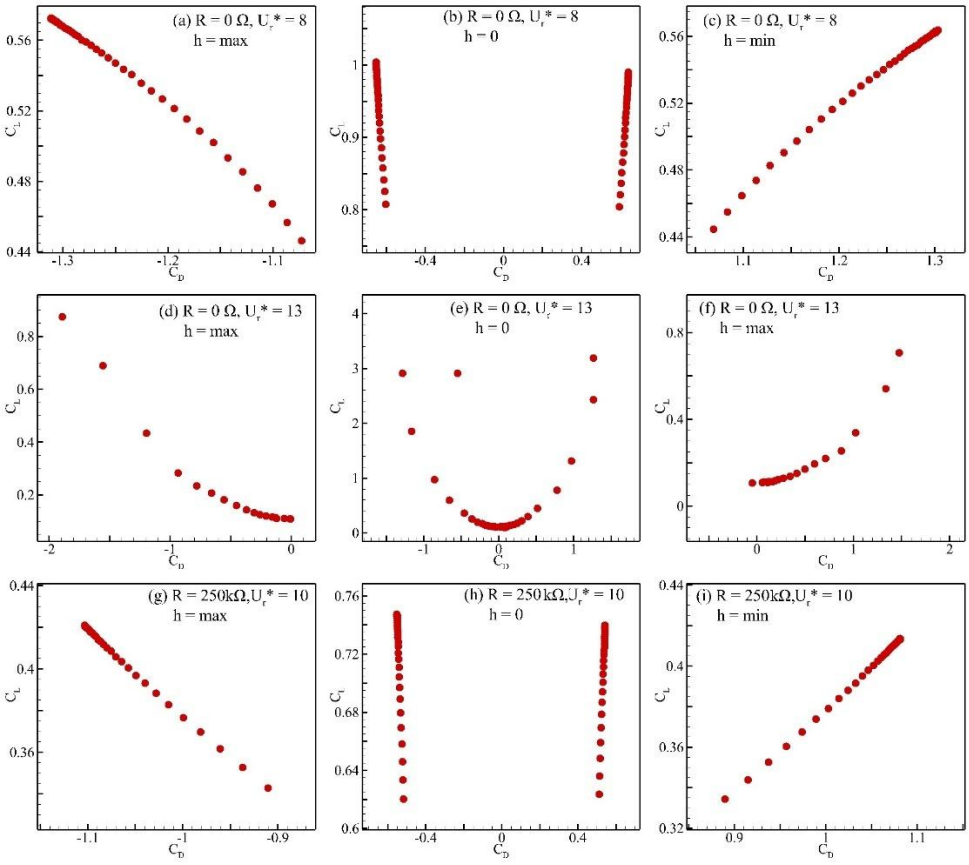

Figure 13: Poincare maps constructed under three different conditions. (a–c), $R = 0\ \Omega$ and U_r^* = 8, showing a periodic nonlinear state. (d–f) , $R = 0\ \Omega$ and U_r^* = 13, where chaotic behavior is observed. (g–i) at $R = 250\ k\Omega$ and U_r^* = 10

In contrast, for higher load resistances such as $\mathrm{R} = 250\ \mathrm{k}\Omega$ (Figures 13g–13i), $\mathrm{R} = 500\ \mathrm{k}\Omega$ (Figures 14a–14c), and $\mathrm{R} = 750\ \mathrm{k}\Omega$ (Figures 14d–14f), the Poincare points converge more gradually. As R increases, the points become more densely clustered, indicating that the system requires significantly more time to transition from the transient regime to a periodic steady state. This behavior underscores the damping effect introduced by the electrical load

resistance, which inhibits the system's progression toward chaotic dynamics. Moreover, both the phase portraits and Poincare maps demonstrate that the system maintains periodic behavior under applied load resistance, whereas in the absence of load, the system transitions to chaos beyond $\mathrm{U_r^*} = 12$ following a crisis route.

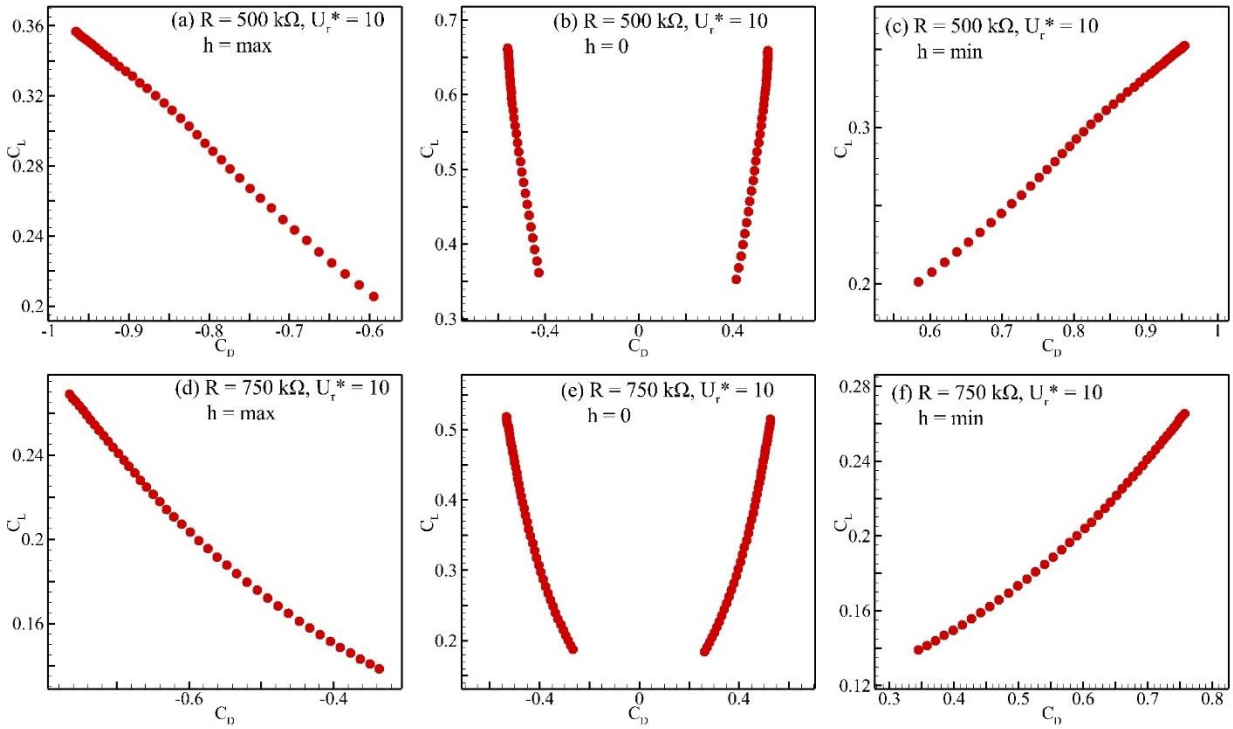

Figure 14: Poincare maps at $R = 500\ k\Omega$ for U_r^* = 10 shown in (a–c) and at $R = 750\ k\Omega$ at U_r^* = 10 shown in (d–f)

Furthermore, the phase maps are generated to characterize the system's dynamic response over the entire range of reduced velocities.

- **Phase map and vortex patterns**

The phase map is plotted to capture the system's behavior over the reduced velocity range $U_r^* = 6$ to 13, as introduced earlier. To further investigate the dynamics at $U_r^* = 13$ with $R = 0$, the results confirm the emergence of chaotic motion via the crisis route, as previously identified through phase portraits and Poincaré maps. Subsequently, a nonlinear solution map on the R and U_r^* is presented in Figure 15**.** For $U_r^* = 6$, the triangle shape in the phase map indicates quasi-nonlinear behavior. As U_r^* increases, the system transitions into a periodic nonlinear regime up to $U_r^* = 12$. Beyond this U_r^*, the response becomes chaotic, marked by a circle for the $R = 0$ case. When $R = 250\ \mathrm{k\Omega}$, the system initially exhibits quasi-nonlinear behavior and transitions to periodic nonlinear oscillations at $U_r^* = 13$. For $R = 500\ \mathrm{k\Omega}$, quasi-nonlinear behavior persists up to $U_r^* = 7$, followed by periodic nonlinear motion, and eventually reverts to quasi-nonlinear dynamics at $U_r^* = 13$. With a further increase to $R = 750\ \mathrm{k\Omega}$, the system shows quasi-nonlinear motion up to $U_r^* = 7$, transitions to periodic nonlinear oscillations up to $U_r^* = 11$, and again returns to quasi-nonlinear behavior. Overall, the phase maps demonstrate that increasing resistance progressively narrows the range of nonlinear responses across reduced velocities, indicating a resistance-induced modulation of the system's nonlinear characteristics, which effectively introduces additional damping.

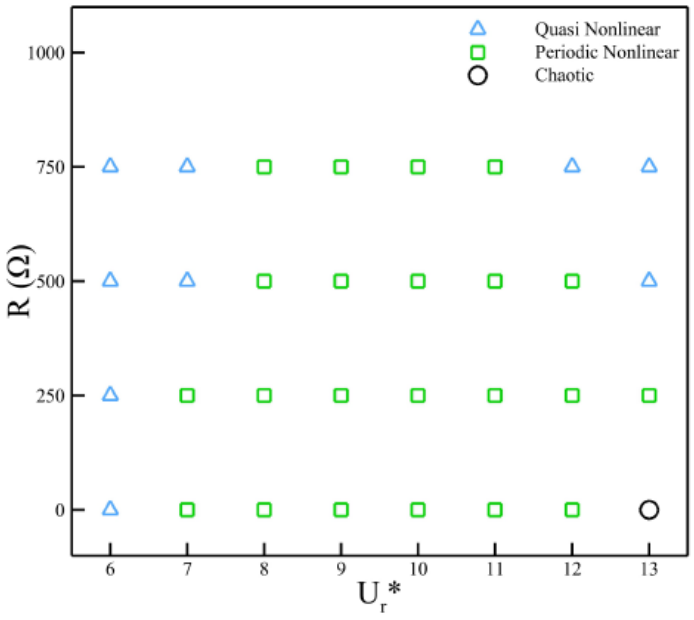

Figure 15: A phase map to illustrate evolution of the systems dynamics with variations in R and U_r^*

To gain deeper insight into the nonlinear states of the system described earlier, we examine the corresponding vortex shedding patterns. Figure 16 presents the phase map, illustrating the flow regimes associated with each half cycle of the oscillating foil. Distinct flow behaviors emerge across different combinations of electrical resistance R and reduced velocity $\mathrm{U_r^*}$. The filled contour regions indicate cases where the shear layer remains attached to the foil surface, producing low-amplitude responses. This is consistent with the small lift coefficients shown in Figure 6 and corresponds to the quasi-nonlinear regime identified in Figure 15.

In Regime 2, the wake transitions to a single-vortex (S) shedding pattern, represented by triangular symbols in the phase map, which aligns with the periodic nonlinear regime in Figure 14. As the flow and system parameters vary further, the wake evolves to exhibit multiple vortex configurations, including single vortices (S), vortex pairs (P), and vortex triplets (T), where three

vortices are shed simultaneously. The coexistence of S, P, and T structures, denoted as multiple pair (mP), signifies an increase in flow complexity and a stronger nonlinear response. These multiple patterns are characteristic of the periodic nonlinear regime in Figure 15.

In the chaotic regime, marked by circular symbol in Figures 15 and 16, the shedding becomes more irregular. The dominant structure remains mP, but additional hybrid configurations, such as P+S, emerge, as identified in Regime 4. This regime reflects the highest degree of nonlinear complexity in the system's wake dynamics.

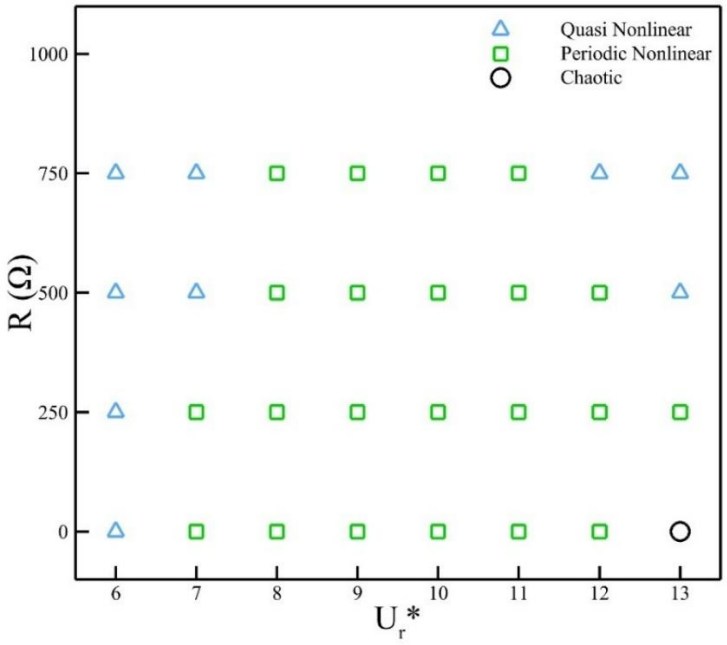

Figure 16: Phase maps show the types of regimes that emerge as R and U_r^* vary. The corresponding vortex shedding patterns observed during a representative half-cycle are marked, highlighting the vortex shedding at different states of nonlinearities.

To further explain the relationship between vortex shedding patterns and the nonlinear behavior of the system, we examine how the wake dynamics evolve with varying $\mathrm{U_r^*}$ and R for

selected cases previously analyzed. For U_r^* ranging from 1 to 6, the shear layer remains attached to the airfoil surface, as also indicated in the phase map in Figure 15, and no significant oscillations are observed. Once the system reaches the critical point identified in Figure 5, vortex shedding initiates at $U_r^* = 7$ for lower resistance values. In this regime, the airfoil exhibits synchronous heaving and pitching motions, producing a single-vortex (S) shedding pattern. As R increases, this S pattern weakens due to load-induced damping.

With further increases in U_r^*, vortex shedding persists in phase with the oscillations, promoting boundary-layer separation under the influence of a strong adverse pressure gradient over the airfoil. This separation intensifies at higher U_r^*, leading to flow structures in each half-cycle that deviate from classical configurations such as the von Kármán vortex street, 2S, or 1P. At larger oscillation amplitudes, the number of shed vortices increases, likely due to reduced effective damping. Correspondingly, the lift coefficient (C_L) spectra displays multiple frequency components, which can be attributed to more vigorous vortex shedding.

In this study, the observed shedding patterns include a range of distinct configurations, such as S, multiple-pair (mP) patterns composed of S, P, and T structures, as well as hybrid mP and P+S patterns, as defined earlier. These observations are consistent with the findings reported by Wang et al. [14].

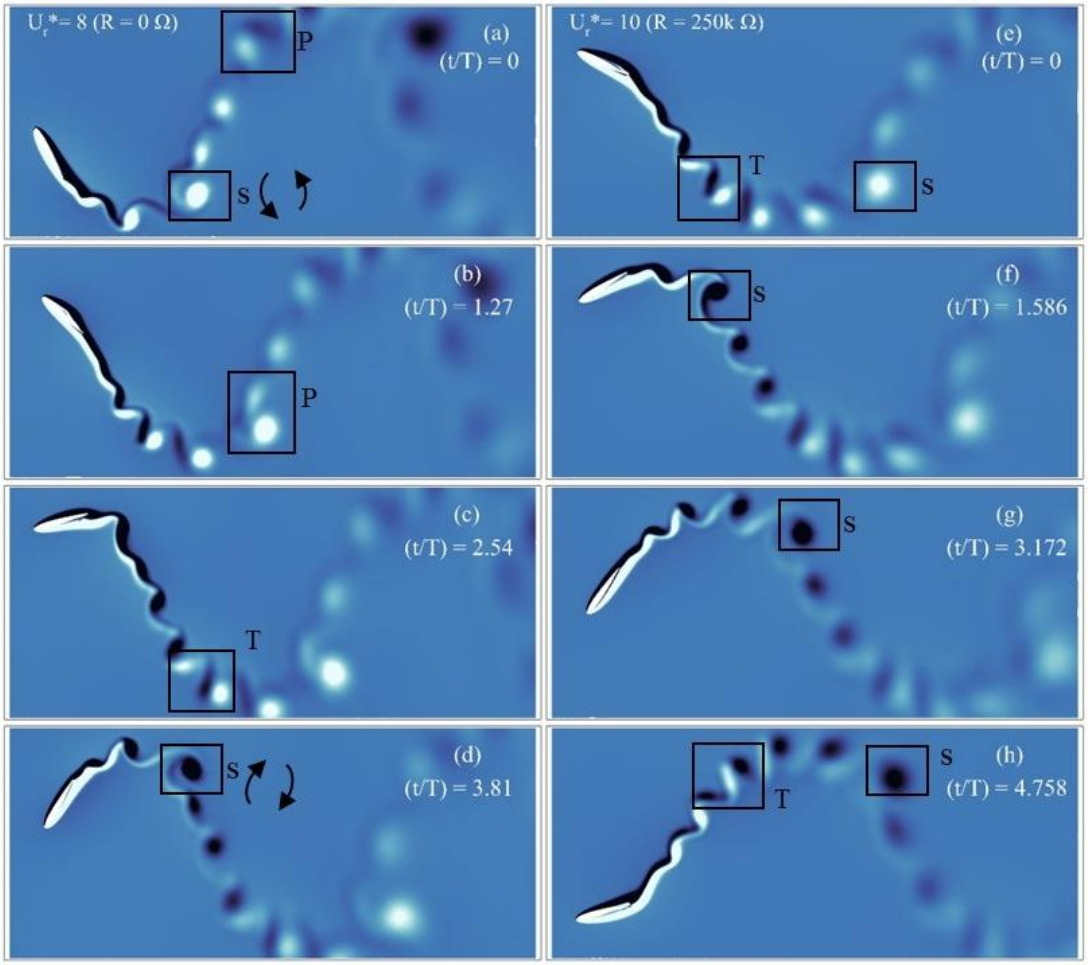

Figure 17: The vortex structures labeled as S, P, and T formed during one half-cycle at (a–d), U_r^* = 8 and $R = 0\ \Omega$ and at (e-h), U_r^* = 10 and $R = 250\ k\Omega$

We now examine selected cases that illustrate representative vortex shedding patterns. At low R and $\mathrm{U_r^*}$, vortex shedding initiates around $\mathrm{U_r^* = 7}$ with a single-vortex (S) pattern. By $\mathrm{U_r^* = 8}$, shedding becomes more vigorous as the airfoil attains larger oscillation amplitudes, fully developing nonlinear characteristics. In this regime, the unsteady aerodynamic response is dominated by rapid variations in the instantaneous angle of attack, leading to delayed flow separation, the formation and shedding of large leading-edge vortices (LEVs), and abrupt

fluctuations in lift and moment coefficients. This phenomenon, observed in Figure 17 and 19 for cases achieving maximum amplitudes, corresponds to dynamic stall.

For the Reynolds number considered in this study, the instantaneous angle of attack during these events exceeds the static stall angle [42]. As shown in Figure 17a, when the foil is in the upstroke, a low-pressure region forms near the leading edge on the suction surface, while the pressure surface experiences comparatively higher pressure. This pressure gradient induces strong suction near the leading edge, initiating the formation of a coherent LEV. As the foil continues to rise, both lift and effective angle of attack increase, causing the LEV to grow in size and strengthen in terms of low-pressure region.

At the peak of the upstroke corresponding to the maximum angle of attack Figure 18, the upper-surface boundary layer can no longer remain attached and detaches near mid-chord due to the rapid reversal of motion. The LEV then rolls up and separates from the foil, producing a sudden drop in lift. In the subsequent downstroke, the LEV convects toward the trailing edge and is partially reattached (recaptured) by the foil, generating a localized low-pressure region and temporarily restoring lift. This vortex recapture also induces a noticeable delay in subsequent vortex shedding, as illustrated in Figure 17 and 19, and is clearly reflected in the temporal lift coefficient profiles in Figure 7**.** At the instant of peak lift, the flow sheds a single-vortex (S) structure, which is subsequently followed by paired (P) and triplet (T) vortices, reflecting a progressive escalation in flow instability.

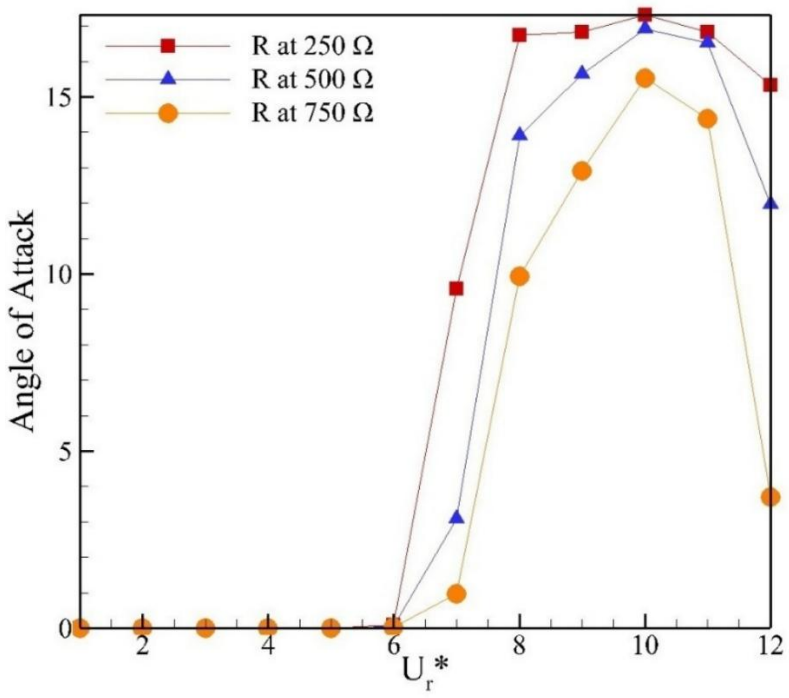

Figure 18: Plots for variations in the effective angle-of-attack of the foil for different values of U_r^* and R

During the upstroke, the airfoil sheds counterclockwise (CCW) vortices, while clockwise (CW) vortices are shed during the downstroke, maintaining symmetry with respect to the stroke direction. Among these, the (S) vortex consistently emerges as the dominant structure in terms of both size and circulation. As previously discussed, the LEV rolls up, detaches, and in some cases reattaches downstream near the trailing edge, where it constructively interacts with a trailing-edge vortex of the same rotational sense. Additional vortices are generated and shed from the trailing edge during the downstroke as the effective angle of attack increases once again. This shedding pattern persists across different resistance values R.

Comparative phase plots show that large amplitude C_L oscillations correspond to the periodic nonlinear regime, which is frequently associated with the mP vortex shedding pattern.

However, as R increases along with U_r^*, the system progressively transitions toward a quasi-nonlinear regime. This trend is also evident in Figures 17 and 19, where vortex activity remains pronounced at lower R but diminishes gradually with increasing R and U_r^*.

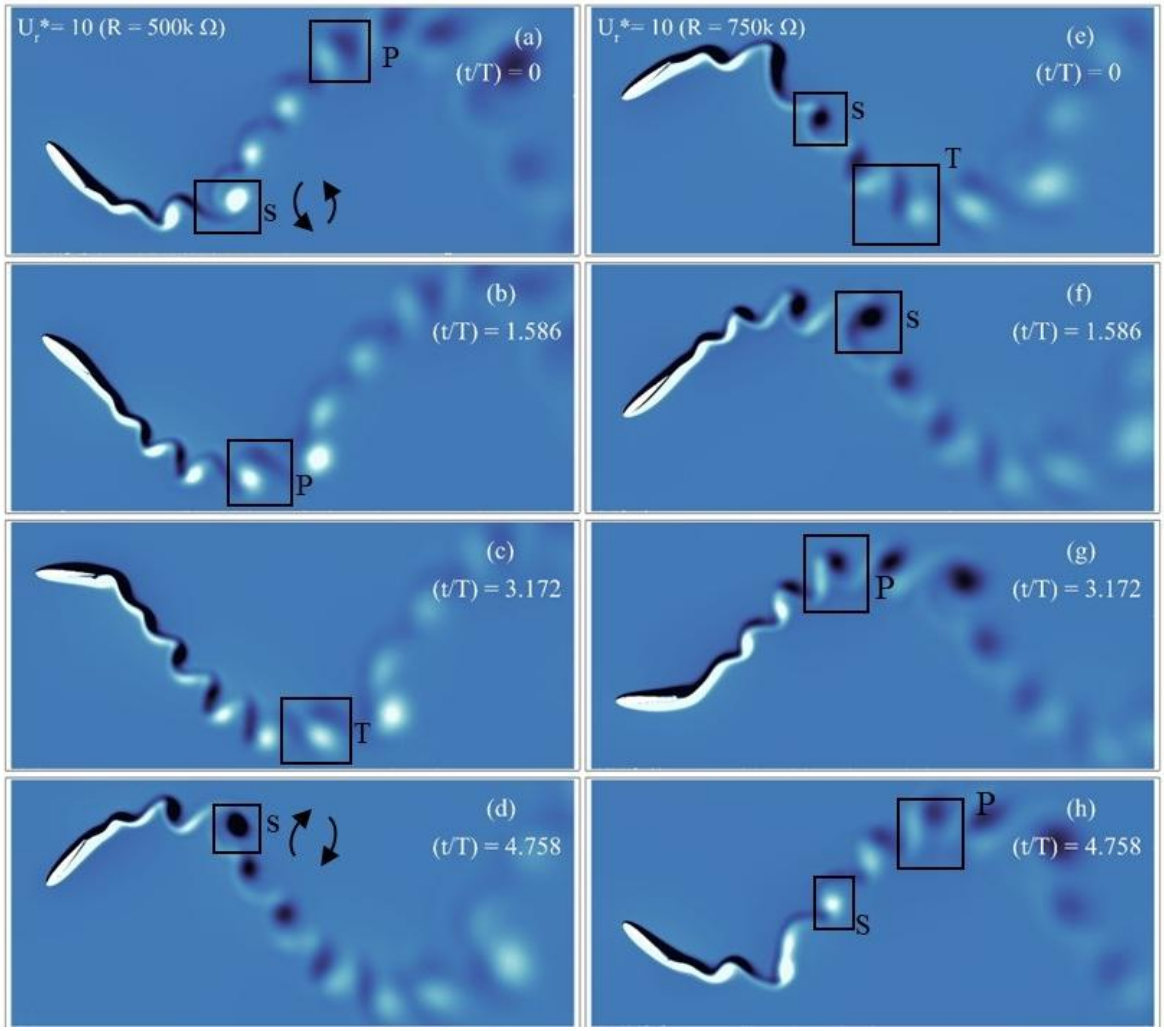

Figure 19: The vortex structures labeled as S, P, and T formed during one half-cycle at (a–d) U_r^* = 10 at $R = 500\ k\Omega$ and at (e–h) U_r^* = 10 for $R = 750\ k\Omega$

For the case with R = 0 and $U_r^* = 13$, which exhibits chaotic behavior, the corresponding vortex pattern is shown in Figure 20. The oscillation amplitude becomes markedly large, with the

detachment of the LEV from the foil surface causing a substantial loss in lift. In this regime, a new vortex-shedding mode emerges, characterized by a hybrid P+S pattern in combination with multiple-pair (mP) vortices. As illustrated in Figure 20a-20f, the LEV undergoes sustained growth in size, reflecting an increase in the aerodynamic forces acting on the structure. This continuous enlargement of the LEV, coupled with intensified vortex interactions, signifies a transition toward a chaotic state driven by progressively increasing unsteady aerodynamic loads.

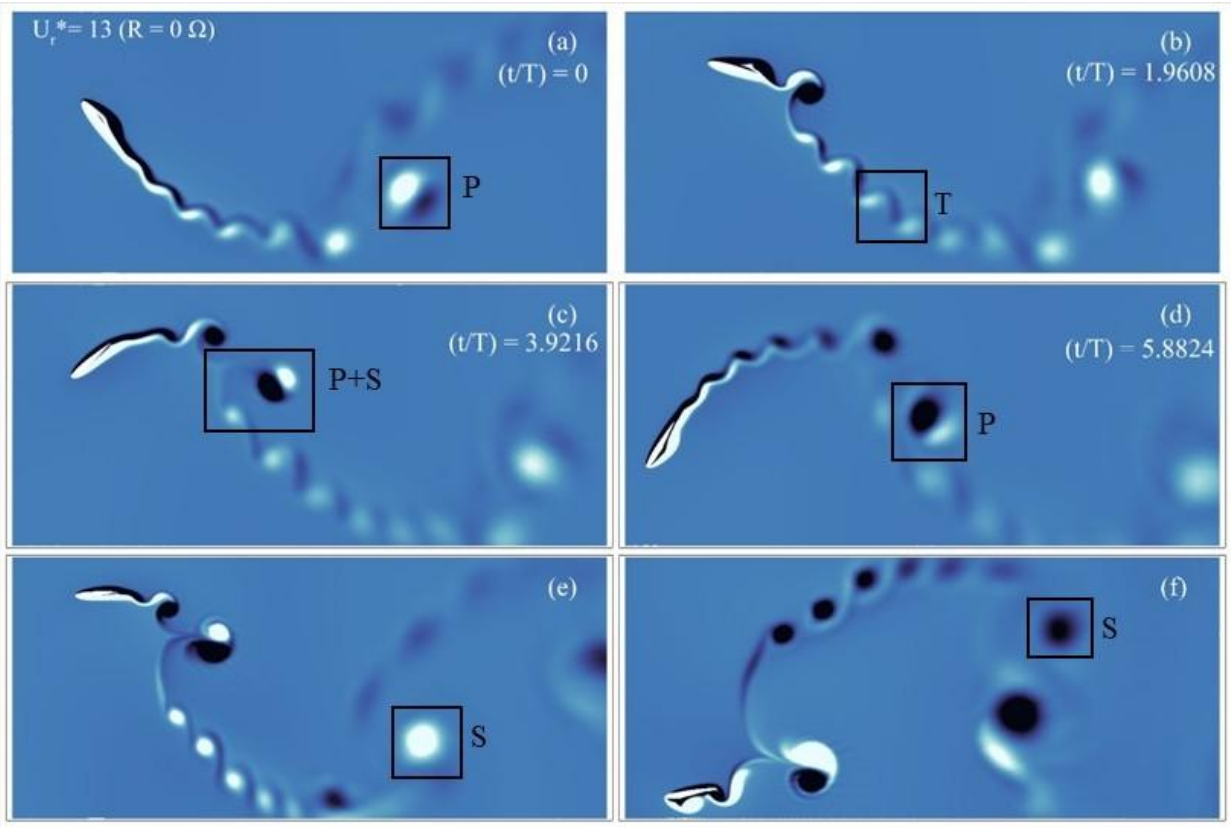

Figure 20: (a–d) Vortex structures labeled as S, P, mP, and P + S formed during one half-cycle at U_r^* = 13 with $R = 0\ \Omega$. (e, f) subsequent variations in the flow field when the foil already begins its downstroke

As discussed earlier, Figure 6 illustrates the variation of C_L with U_r^*, showing that the bifurcation region narrows with increasing electrical resistance R. This behavior indicates that higher resistive loading progressively limits the onset and growth range of oscillations due to enhanced damping effects.

The analysis is further extended to the electrical response of the system, focusing on the voltage output during the onset of oscillations, the attainment of maximum amplitude, and across varying U_r^* and R. The non-dimensional voltage (V^*), is computed at each time step by the solver, and once the system reaches a steady oscillatory state, the root-mean-square (RMS) value V_{RMS}^* , is evaluated using the formulation outlined in subsection 2.2. Figure 20 presents V_{RMS}^* as a function of reduced velocity. The voltage profile follows the bifurcation pattern observed in the dynamic response (see Figure 6 for C_L vs. U_r^*), with larger oscillation amplitudes of C_L corresponding to higher voltage outputs through the piezoelectric coupling mechanism.

The results also show how voltage generation varies with both U_r^* and R. Comparison with the phase portraits (Figures 12a, 12d, and 12g) and vortex shedding patterns (Figures 17 and 19) reveal that higher voltage outputs coincide with cases exhibiting larger vortex shedding activity and nonlinear periodic behavior in the structural response. Conversely, as the system transitions toward a quasi-nonlinear state, both vortex shedding intensity and voltage amplitude decrease, indicating reduced energy transfer from the fluid to the structure. From the voltage profiles, it is also evident that the highest electrical output occurs at larger R values and at U_r^* corresponding to the maximum C_L.

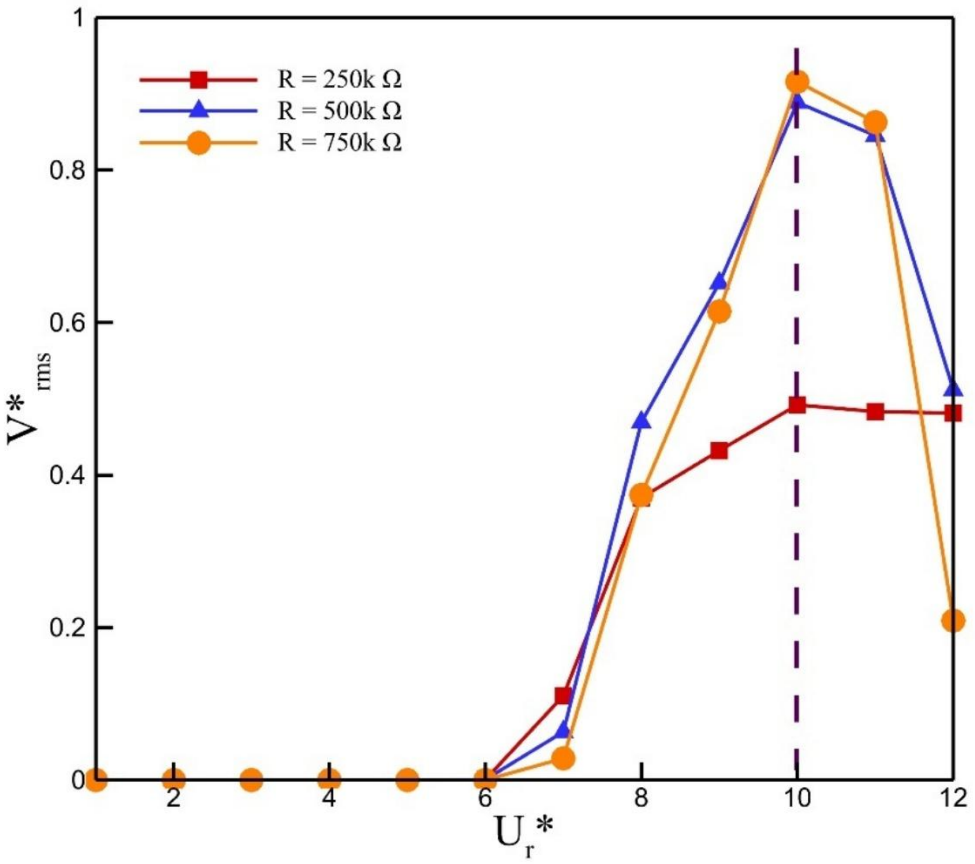

Figure 21: RMS voltage (V^*) as a function of reduced velocity (U_r^*) for various load resistances

Chapter 4: Three-Dimensional Fluid-Structure-Electrical Interactions

In this chapter, the influence of nonlinear dynamics and vortex mechanics on energy harvesting is examined for varying spanwise lengths in the third dimension. Three spanwise lengths (0.3c, 0.6c, and 0.9) are considered for the 3D fluid-structure-electrical interactions. CFD computations are carried out, with all other parameters kept consistent with the 2D configuration. The only variation lies in the number of nodes in the spanwise (z) direction, which are set to 24, 48, and 72 for the respective spanwise lengths. This section presents an analysis of the system's response through temporal-history plots, FFT spectra, phase portraits, Poincare maps, and vortex visualizations.

By plotting the heaving amplitude (h^*), pitching angle (θ), lift coefficient (C_L), and drag coefficient (C_D) versus time, the results from 2D simulations are compared with the those from the 3D simulation at the corresponding parameters. The distinctions between the different signals are indicated in the legend of the figures. The first comparison is performed at $R = 250\ k\Omega$ for all three spanwise lengths in Figure 22. The results from the 2D simulations show higher oscillation amplitudes across all quantities, whereas those from 3D simulations with the smallest span (0.3c) are completely damped, showing negligible oscillations. The results for the span of 0.6c exhibit moderate oscillations, while C_L and C_D for the span of 0.9c closely follow the trends observed in the 2D results, indicating that the 2D system effectively captures the dynamic characteristics of the 3D system with the largest span considered here.

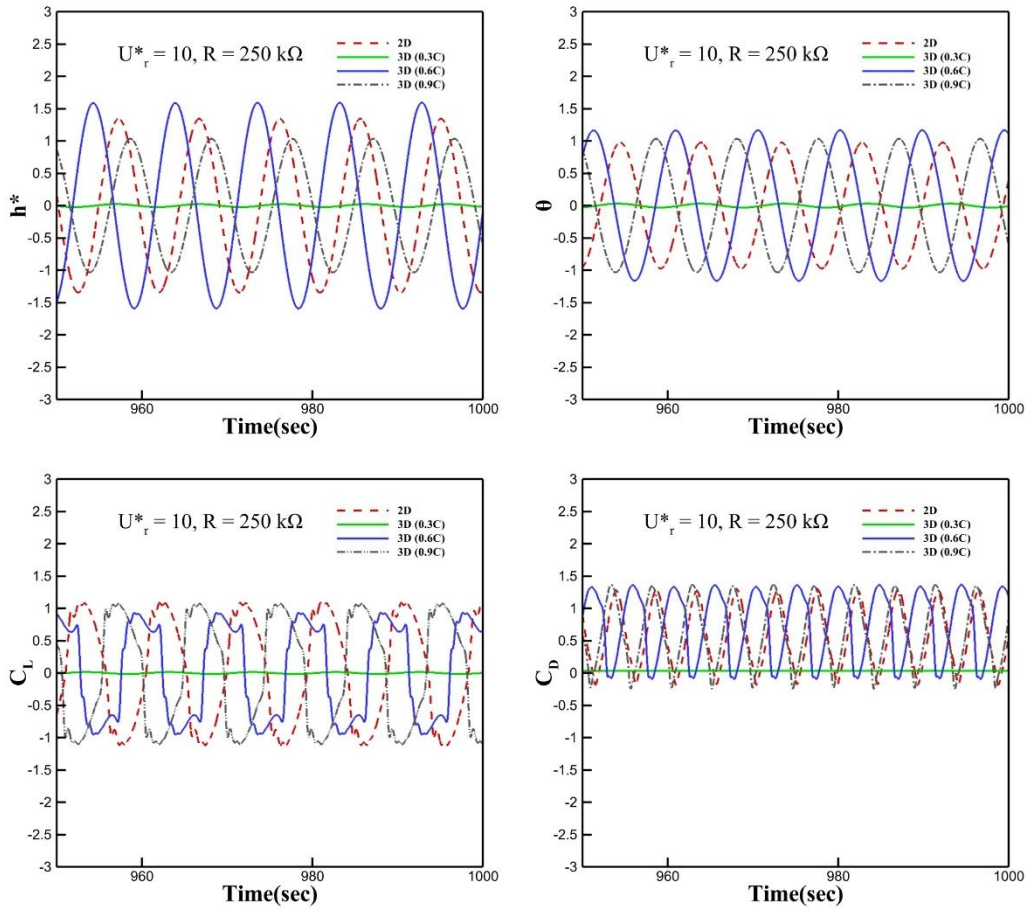

Figure 22: Comparison of heaving amplitude (h^*), pitching angle (θ), lift coefficient (C_L), and drag coefficient (C_D) at U_r^* = 10 and $R = 250\ k\Omega$ for different spanwise lengths

When the load resistance is increased to $\mathrm{R} = 500\ \mathrm{k\Omega}$, the behavior observed in all the plots, provided in Figure 23, is similar to that seen at $\mathrm{R} = 250\ \mathrm{k\Omega}$. The $\mathrm{C_L}$ and $\mathrm{C_D}$ signals for the 0.9c span continue to closely match with the 2D results. From these plots, the peak-to-peak variations in $\mathrm{C_L}$ exhibit slight non-smoothness, indicating the presence of nonlinear behavior in the system. Additionally, the signals are skewed towards the left-hand side, highlighting the presence of asymmetry in the aerodynamic response.

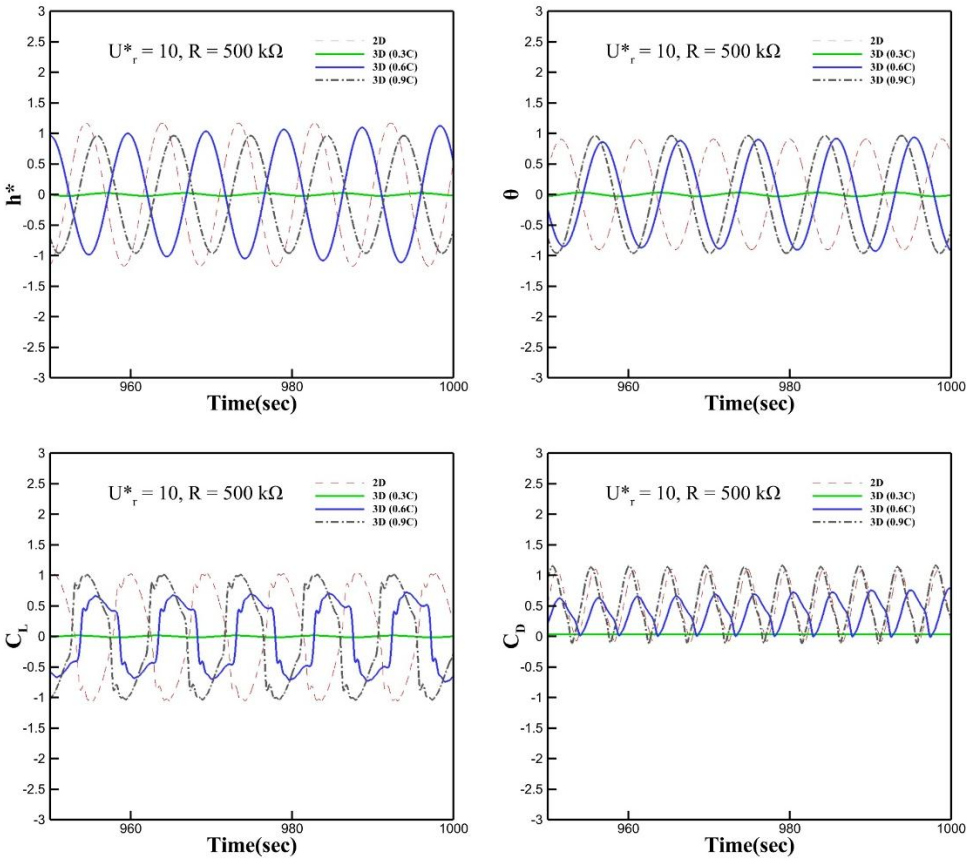

Figure 23: Comparison of heaving amplitude (h^*), pitching angle (θ), lift coefficient (C_L), and drag coefficient (C_D) at U_r^* = 10 and $R = 250\ k\Omega$ for different spanwise lengths

As the load resistance is further increased at $750\ \mathrm{k\Omega}$ and again $\mathrm{h^*}$, θ, $\mathrm{C_L}$, and $\mathrm{C_D}$ are compared with the 2D results in Figure 24, the span length of 0.9c continues to closely match the behavior of the corresponding 2D system, particularly in terms of $\mathrm{C_L}$ and $\mathrm{C_D}$. From these comparisons, it is evident the response of the oscillating wing with a span of 0.9c consistently exhibit the closest agreement with the 2D configuration, while the smaller span lengths (0.3c and 0.6c) show reduced amplitudes and less similarity to the 2D configuration.

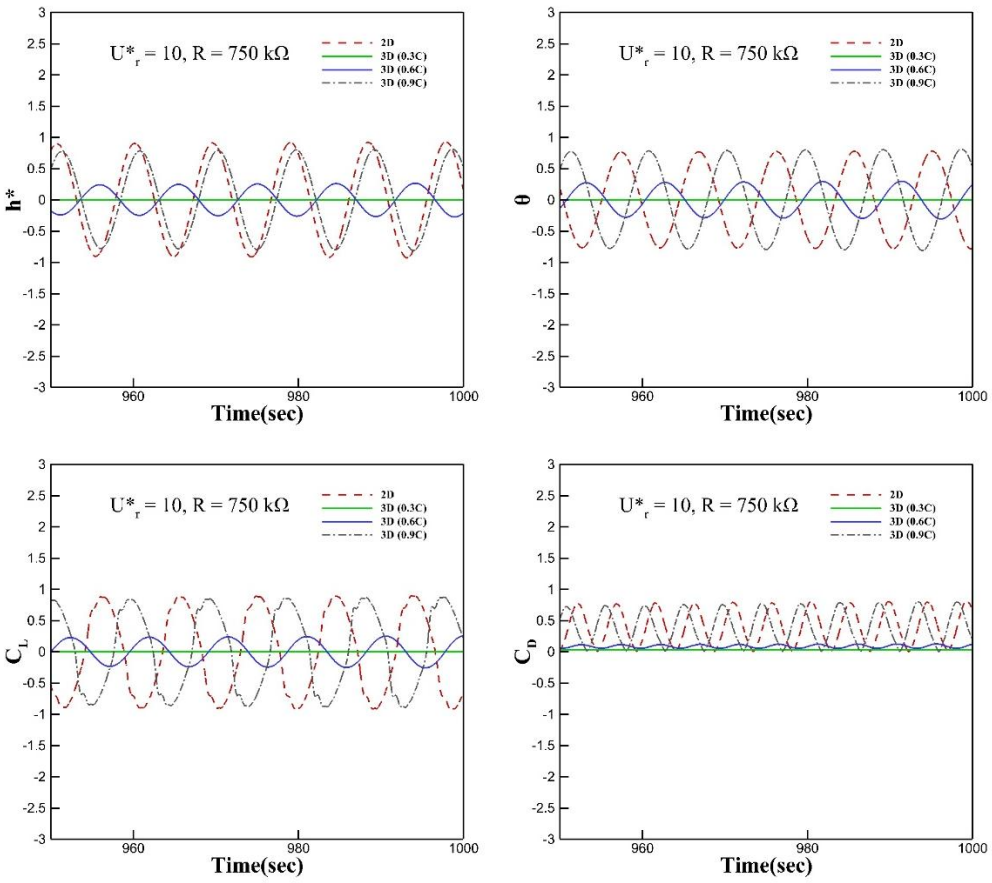

Figure 24: Comparison of heaving amplitude (h^*), pitching angle (θ), lift coefficient (C_L), and drag coefficient (C_D) at U_r^* =10 and $R = 750\ k\Omega$ for different spanwise lengths

- **Temporal-history plots of C_L**

Using the $\mathrm{C_L}$ response at $\mathrm{U_r^* = 10}$, temporal-history plots ae generated for each spanwise length (0.3c, 0.6c, and 0.9c). Figures 25a–25c for $\mathrm{R = 250\ k\Omega}$, represents the $\mathrm{C_L}$ signal at different spans, in which Figure 25a exhibits very small oscillation amplitudes with a symmetric signal as we move towards the higher span of 0.6c (see Figure 25b), the amplitude increases, and the signal becomes non-smooth between successive peaks, indicating the presence of nonlinearity. Increasing the span further to 0.9c shown in Figure 25c, results in an even larger

amplitude, along with a distinct left-skewness of the signal, signifying the presence of asymmetry. For $\mathrm{R} = 500\ \mathrm{k\Omega}$, the span lengths in Figure 25d-25f exhibit similar qualitative trends to those observed in the plots for $\mathrm{R} = 250\ \mathrm{k\Omega}$. Besides, the oscillation amplitudes are noticeably reduced, reflecting the damping effect of higher electrical load resistance as well.

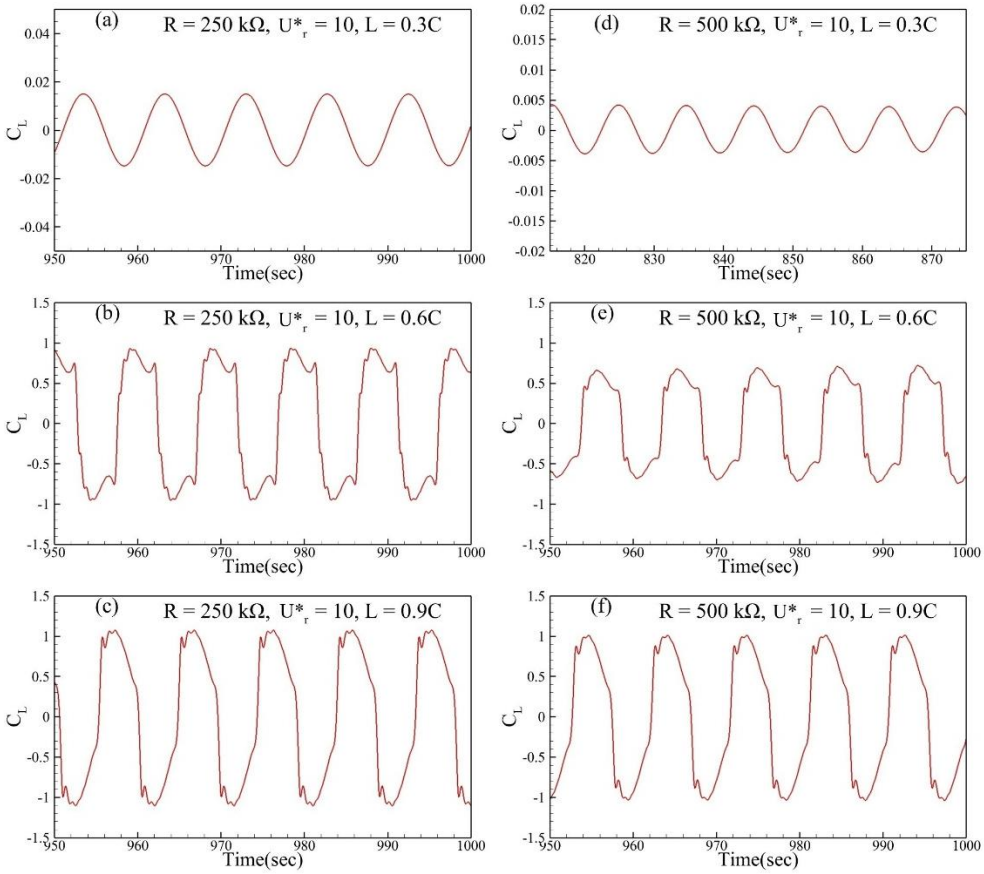

Figure 25: Temporal histories of C_L at U_r^* = 10 and R = 250 kΩ and 500 kΩ at 0.3c, 0.6c and 0.9c

In Figures 26g–26h, for $\mathrm{R} = 500\ \mathrm{k\Omega}$ at different spans, a similar trend is observed for the wing with a span of 0.3c, the oscillation amplitude of $\mathrm{C_L}$ remains very low. However at 0.6c, the amplitude increases. For the wingspan of 0.9c, the amplitude approaches nearly unity. At $\mathrm{R} = 750\ \mathrm{k\Omega}$ and span of 0.9c in Figure 26i has same trends as compared to other two load resistances

in Figures 25c and 25f. Therefore, by seeing this behavior and is consistent with all previously examined 0.9c cases across different load resistances and closely matches the pattern observed in Figure 7 of the 2D results at various load resistance values. From this, it can be concluded that the 0.9c 3D results at $U_r^* = 10$ are in close agreement with the 2D analysis outcomes. To further investigate the nature of the nonlinearity, as well as the presence of asymmetry and higher harmonics, FFT analyses are subsequently performed for all three spanwise length across different R.

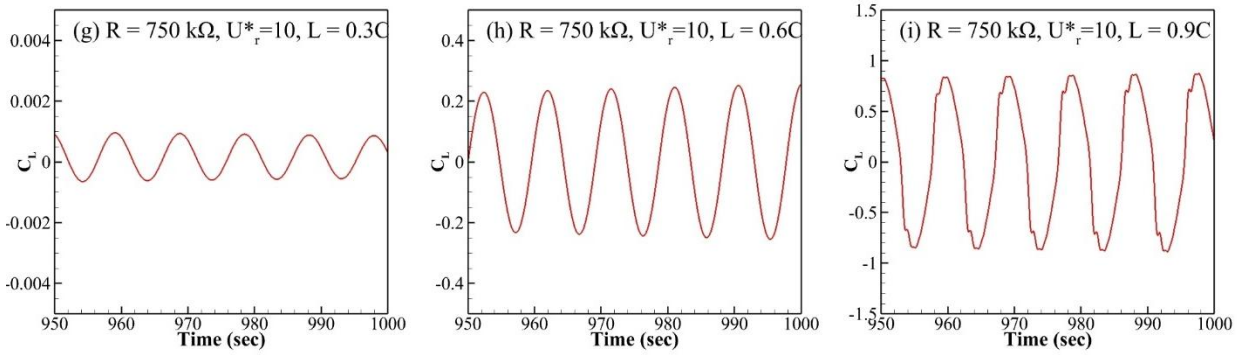

Figure 26: Temporal histories of C_L at U_r^* = 10 and R = 750 kΩ at 0.3c, 0.6c and 0.9c

- **Fast Fourier-Transform plots**

In the FFT analysis, the spectral distributions for different spans and load resistances are examined. Figures 27a–27c shows the spectra for C_L of the wing with 0.3c span at $R = 250\ k\Omega$. In Figure 27a, the spectrum exhibits only a single peak corresponding to the fundamental frequency, with no observable subharmonics or superharmonics. It indicates a predominantly linear system response for the wing with 0.3c span, consistent with the symmetric wave observed earlier in Figure 27a. However, when the span is increased to 0.6c and 0.9c (see Figures 29b-29c), additional peaks appear at integer multiples of the fundamental frequency, indicating the

presence of quadratic and cubic nonlinearities. The occurrence of quadratic harmonics suggests asymmetry in the system response. At $\mathrm{R} = 500\ \mathrm{k}\Omega$,similar trends are observed in Figure 27d shows that the rersponse from the 0.3c wingspan remains linear with only the fundamental frequency present, while Figure 27e and 27f for the spans of 0.6c and 0.9c reveals the presence of superharmonics and with no subharmonics, again indicating nonlinear behavior. Overall, the FFT results confirm that both load resistances exhibit consistent spectral trends, with nonlinear effects becoming more pronounced as the span increases.

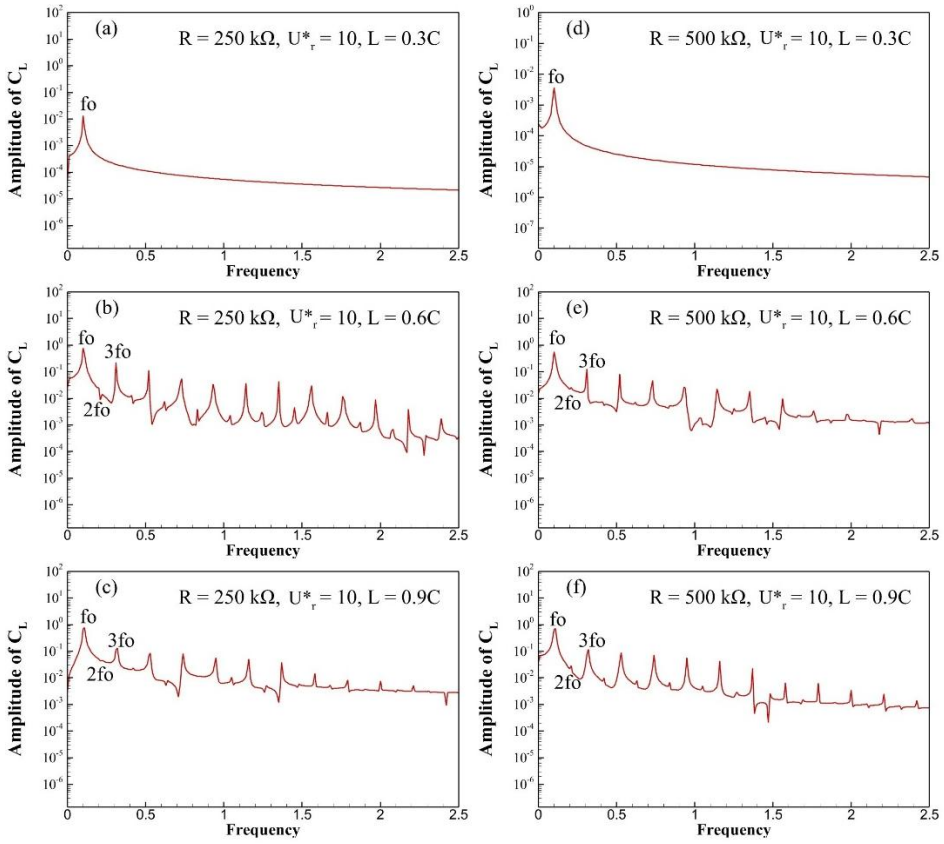

Figure 27: Spectra of C_L at $R = 250\ k\Omega$: (a–c) and $R = 500\ k\Omega$: (d–f) for U_r^* = 10 at different spanwise length

At $R = 750\ k\Omega$, the spectra in Figures 28g–28i show that for 0.3c and 0.6c span (see Figure 28g-28h), the response is characterized solely by a single peak at the fundamental frequency, indicating a predominantly linear system behavior at these spanwise lengths. In contrast, for 0.9c span in Figure 28i, the spectrum contains both the fundamental frequency and distinct superharmonics, signifying the presence of nonlinear dynamics. A comparison of the spectral trends in Figures 27 and 28 reveals that the 0.9c configuration consistently displays nonlinear characteristics across all load resistances, showing strong similarity to the FFT peak patterns observed in the 2D configuration at $U_r^* = 10$ (see Figures 8 and 9). By these observations, phase portraits are subsequently generated for the 0.9c span at different R. These portraits illustrate the system's state-space evolution over time, offering a clearer understanding of its dynamical behavior, and nature of nonlinearity, and the influence of load resistance on the trajectory characteristics. For completeness, the dominant frequencies extracted from both the 2D and 3D simulations results are summarized in the accompanying table, enabling a direct quantitative comparison.

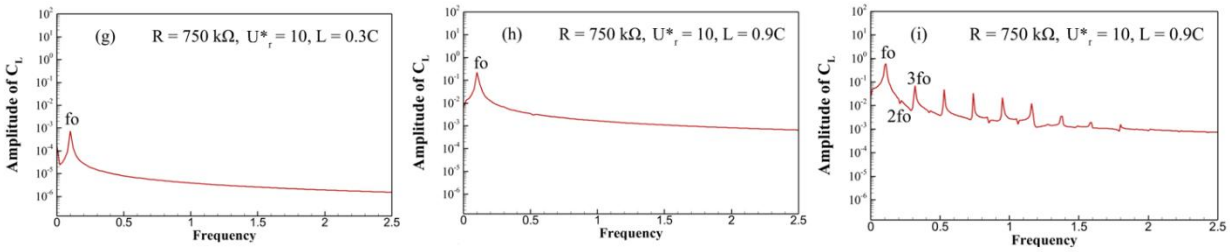

Figure 28: Spectra of C_L at R = 750 kΩ: (g–i) for U_r^* = 10 at different spanwise length

Table 7: Natural structural frequency and fundamental frequency of 2D and 3D results

	Natural Structural Frequency (Hz)	**Fundamental Frequency (Hz)**		
Simulations\ Resistances		250 kΩ	500 kΩ	750 kΩ
2D	0.10000	0.1050	0.1050	0.1050
3D (0.3c)	0.10000	0.0999	0.0999	0.0999
3D (0.6c)	0.10000	0.0999	0.0999	0.0999
3D (0.9c)	0.10000	0.1099	0.1099	0.1099

- **Phase portraits**

From the above analysis, phase portraits are constructed for $\mathrm{R} = 250, 500 \text{ and } 750\ \mathrm{k\Omega}$, corresponding to the 0.9c span. As shown in Figure 29a for $\mathrm{R} = 250\ \mathrm{k\Omega}$, the trajectory in state space is very thin and tightly bound, indicating that the system repeatedly follows the same closed path over time. This behavior is characteristic of a periodic nonlinear response that has reached a stable LCO. In such a state, the oscillations of both $\mathrm{C_L}$ and $\mathrm{C_D}$ remain consistent in amplitude and phase, and the system dynamics are highly repeatable from cycle to cycle. In Figure 29b, corresponding to $\mathrm{R} = 500\ \mathrm{k\Omega}$, the trajectory loop becomes noticeably thicker compared to the $\mathrm{R} = 250\ \mathrm{k\Omega}$ phase portraits. This thickening suggests slight variations in the state-space path over time, pointing to changing in the oscillations. Additionally, the amplitude of both $\mathrm{C_L}$ and $\mathrm{C_D}$ decreases relative to the higher resistance, reflecting the damping effect of the electrical load. Similar thickening is observed in Figure 29c for $\mathrm{R} = 750\ \mathrm{k\Omega}$, but here the effect is more pronounced. The loop shape remains broadly similar to the lower R results, but the oscillation amplitudes are further reduced, and the trajectory becomes less consistent from

one cycle to the next. Across all three load resistances, the phase portraits exhibit asymmetry, with the loops biased toward the positive C_D side of the plot. This asymmetry indicates that the mean drag is nonzero. Furthermore, the structure of the loops clearly demonstrates that the dominant frequency of C_D is approximately twice that of C_L. Specifically, a complete loop in the portrait corresponds to a single C_L cycle, while each half-loop corresponds to a C_D cycle. When comparing these 3D and 2D results shown in Figures 29d-29f, the phase portrait patterns are remarkably consistent, exhibiting similar loop geometries and asymmetry. However, the effect of increasing load resistance is also evident in the 3D simulations, particularly in Figure 29c, where the system does not follow its trajectory and the oscillation amplitudes gradually decay over time. This indicates that, at higher load resistances, the system transitions from a periodic nonlinear regime toward a quasi-nonlinear state, with reduced coherence in its oscillatory behavior and not going toward the chaos. To further analyze the behavior depicted in these plots and determine whether the system exhibits nonlinear periodicity, quasi-periodicity, or chaos.

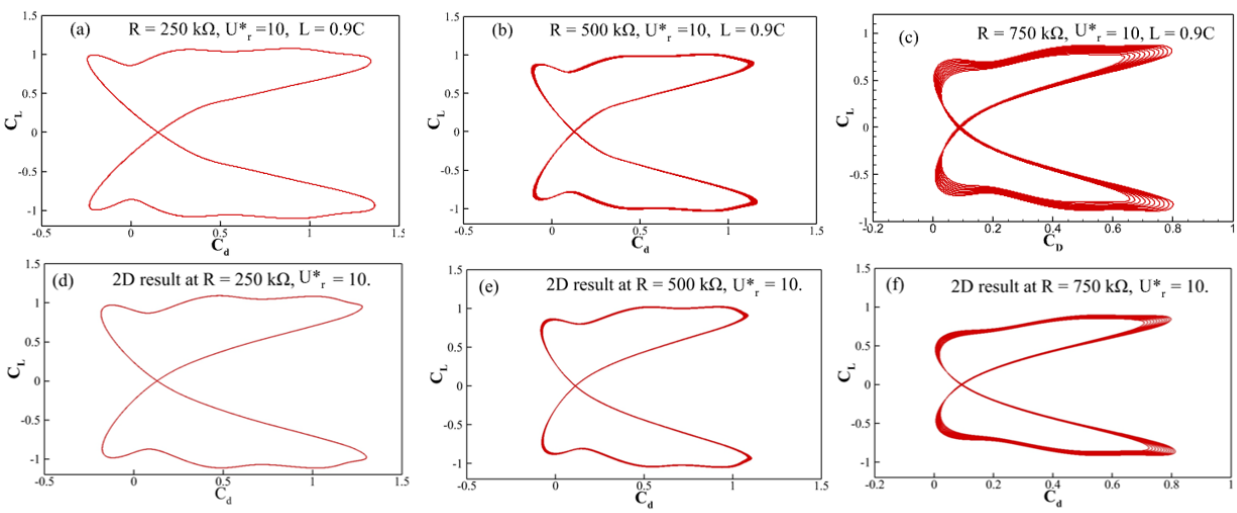

Figure 29: Comparison of 3D phase portraits at 0.9c with corresponding 2D results across different load resistances

- **Poincare maps**

In this section, we present a detailed comparison between the 3D results obtained for an span of 0.9c and the corresponding 2D results at various load resistances, focusing on the Poincare maps to assess the system's nonlinear dynamical states. At $\mathrm{R} = 250\ \mathrm{k}\Omega$ in Figure 30a, the Poincare points are initially positioned with a noticeable separation, indicating the quasi-nonlinear state in the early stage. As the lift coefficient $\mathrm{C_L}$ gradually increases, the points begin to cluster closer together, and with further evolution, they eventually overlap. This progression signifies that the system transitions into a periodic nonlinear regime and settles into limit cycle oscillations. These observations are consistent with the phase portrait results, which also display closed, stable loops corresponding to periodic nonlinear state. For $\mathrm{R} = 500\ \mathrm{k}\Omega$ in Figure 30b, the Poincare points start with smaller initial spacing compared to $\mathrm{R} = 250\ \mathrm{k}\Omega$. As the system evolves over time, the separation between points increases during intermediate stages before decreasing again, leading to eventual overlapping. This behavior suggests that the system reaches a periodic nonlinear state, but with a reduced oscillation amplitude in $\mathrm{C_L}$. The smaller amplitude and intermediate spacing variation point toward the influence of electrical damping introduced by the higher load resistance, which suppresses oscillation energy without fully disrupting the periodic nature of the motion.

At $\mathrm{R} = 750\ \mathrm{k}\Omega$ in Figure 30c, the Poincare points are separated by an almost constant distance, even for higher $\mathrm{C_L}$ values and not overlap only moving slightly closer. This pattern indicates that the system is no longer retracing the same trajectory in state space. Instead, as the oscillations evolve, the system gradually drifts toward a new trajectory with thicker loop indicates the system is going towards the quasi-nonlinear state. The slow convergence of the points and the absence of closed loops in the phase space are signs of increased damping effects from the electrical load. Also, when comparing these findings with the 2D results in Figure 30d-30f, a strong qualitative similarity emerges all load resistances, where both the 2D and 3D systems maintain periodic nonlinear oscillations and limit cycles, with reduced amplitudes at higher resistances. From the Poincare maps, it is evident that the 3D results for an span of 0.9c closely match the 2D results, confirming the consistency of the observed nonlinear behaviors across all compared results. To further investigate how vortex dynamics and nonlinearity are interconnected in the 3D results, a detailed discussion is provided in the following section.

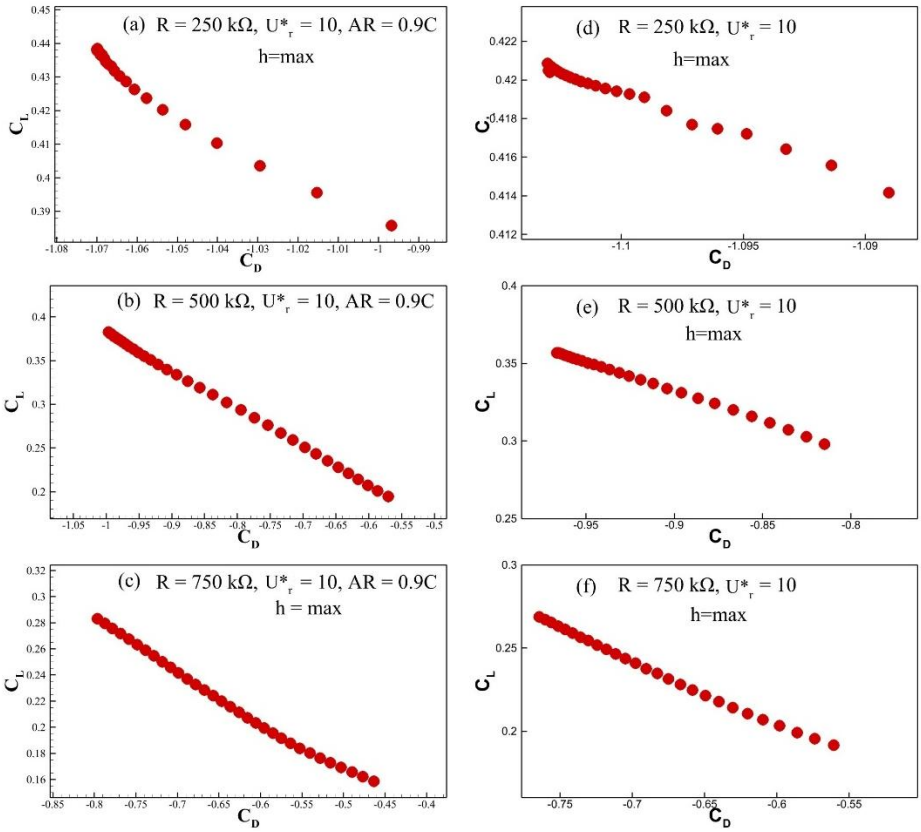

Figure 30: Poincare maps of 3D results at 0.9c and U_r^* = 10 with comparison to 2D results at different load resistances

- **Vortex mechanics**

In this section, we discuss the vortex dynamics and their connection to the observed nonlinear behavior, while also comparing the 3D results for spanwise length of 0.6c and 0.9c at $\mathrm{U_r^*} = 10$ with the corresponding 2D results at different load resistances.

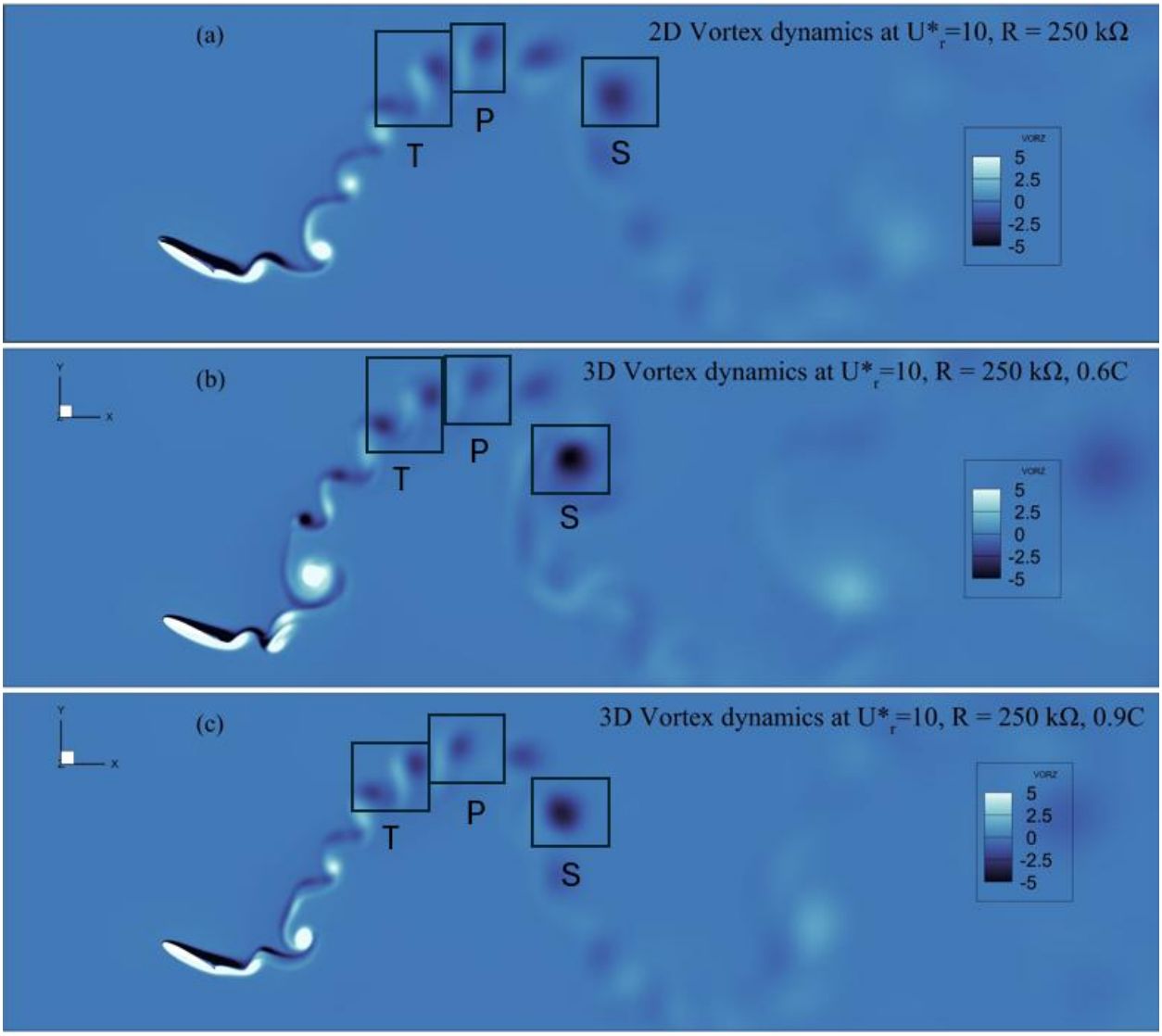

Figure 31: Comparison of 2d vortex dynamics at U_r^* = 10 and 3d vortex dynamics at different spanwise length and $R = 250\ k\Omega$

In Figure 31a at $\mathrm{R} = 250\ \mathrm{k\Omega}$, represents the 2D vortex dynamics, while Figure 31b-31c show the 3D vortex dynamics for span 0.6c and 0.9c, respectively. A direct comparison with the 2D results reveals that the 3D simulations exhibit a similar vortex shedding sequence: as the foil transitions from upstroke to downstroke, it first sheds a single (S) vortex, followed by a pair (P),

and then a triplet (T). The same sequence is repeated during the downstroke-to-upstroke transition. This combination of S-P-T structures corresponds to a multiple-pattern (mp) vortex shedding mode, which is typically observed only at higher oscillation amplitudes in terms of C_L .

The vortical structures illustrated in the figure represent half a cycle of motion. Notably, the 3D results for both 0.6c and 0.9c span lengths capture similar (mp) shedding, with even similar aggressive vortex formation compared to the 2D case. When these shedding patterns are correlated with the FFT maps at the same parameters, it emerges, the presence of such complex vortex shedding coincides with nonlinear system behavior, as evidenced by the appearance of multiple spectral peaks (superharmonics) alongside the fundamental frequency. Furthermore, the more intense the vortex shedding activity, the greater the number of superharmonic peaks observed.

As the load resistance increases to $R = 500\ k\Omega$, a comparison between the 2D and 3D results Figure 32 again reveals the presence of the same multiple vortices shedding patterns which we observed at lower resistances. This indicates that the fundamental vortex shedding mechanism remains unchanged across both the resistance. However, the amplitude of the oscillations particularly in the lift coefficient C_L is reduced, and the overall vortex shedding activity becomes noticeably weaker. The reduction in vortex activity strength and frequency peaks suppressing with the damping effect introduced by the higher electrical load, which also suppresses the oscillations while still preserving the general pattern of vortex formation.

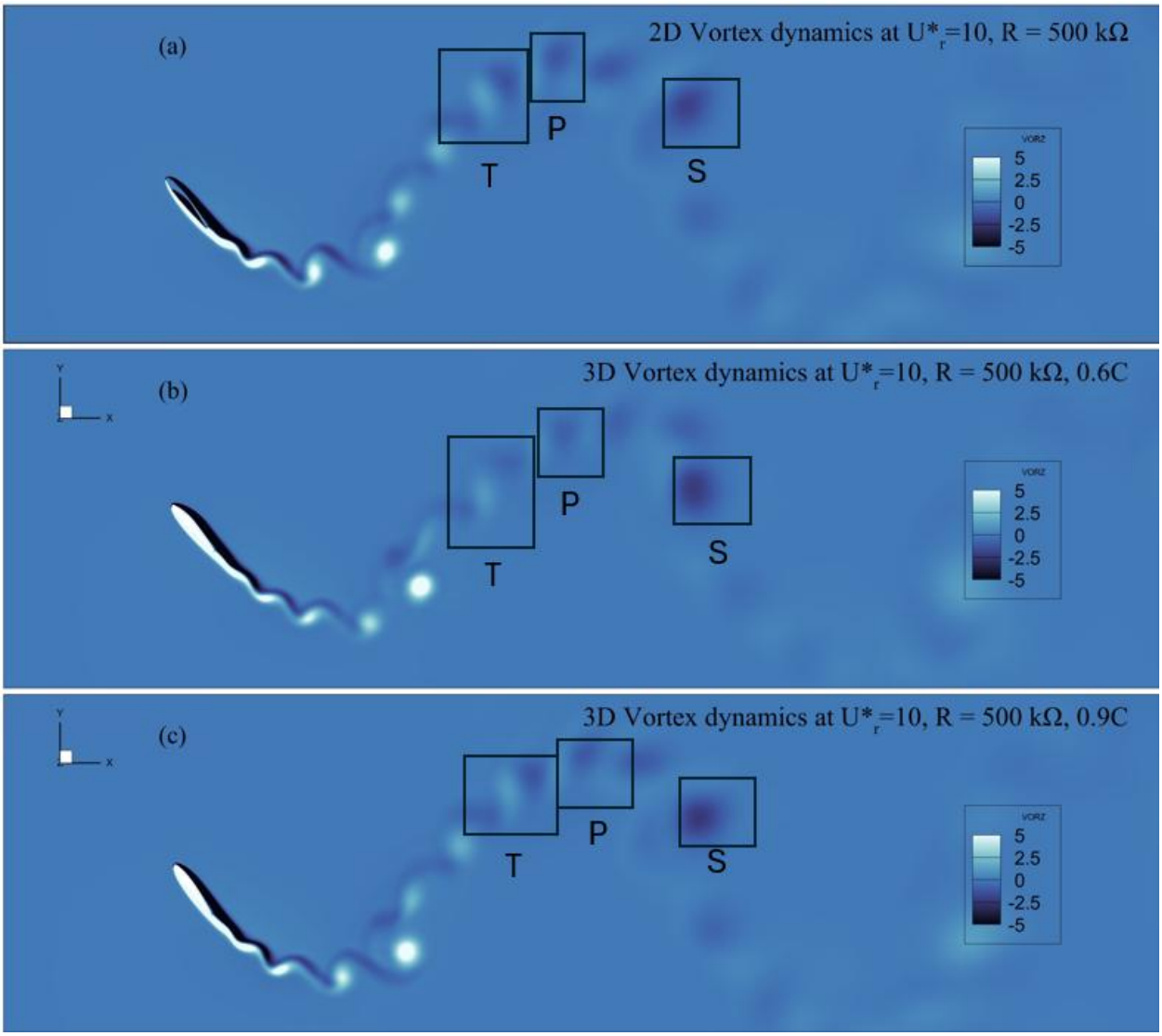

Figure 32: Comparison of 2d vortex dynamics at U_r^* = 10 and 3d vortex dynamics at different spanwise length and R = 250 kΩ

However, as we move to $\mathrm{R} = 750\ \mathrm{k}\Omega$, the 2D results in Figure 33a still display multiple vortex shedding patterns (mP). In contrast, the span of 0.6c, shown in Figure 33b, exhibits a significant reduction in vortex shedding intensity, with predominantly P-type (pair) vortices being shed. This weakening of the shedding pattern is reflected in the corresponding FFT spectrum,

where only a single dominant frequency is present and no superharmonics are observed, indicating a largely periodic response with minimal nonlinear interactions. The lift coefficient (C_L) amplitude is also notably reduced.

In the 0.9c of span, shown in Figure 33c, the vortex shedding activity becomes more pronounced again, with multiple shedding patterns re-emerging. The associated FFT spectrum clearly displays multiple peaks, including higher-order harmonics, suggesting that the system has regained a nonlinear response at this span despite the higher load resistance. However, across all three comparisons in the vortex mechanics section, the 3D vortex dynamics at span of 0.9c closely match the 2D vortex dynamics results, a consistency that is also evident in the phase portraits and Poincare maps.

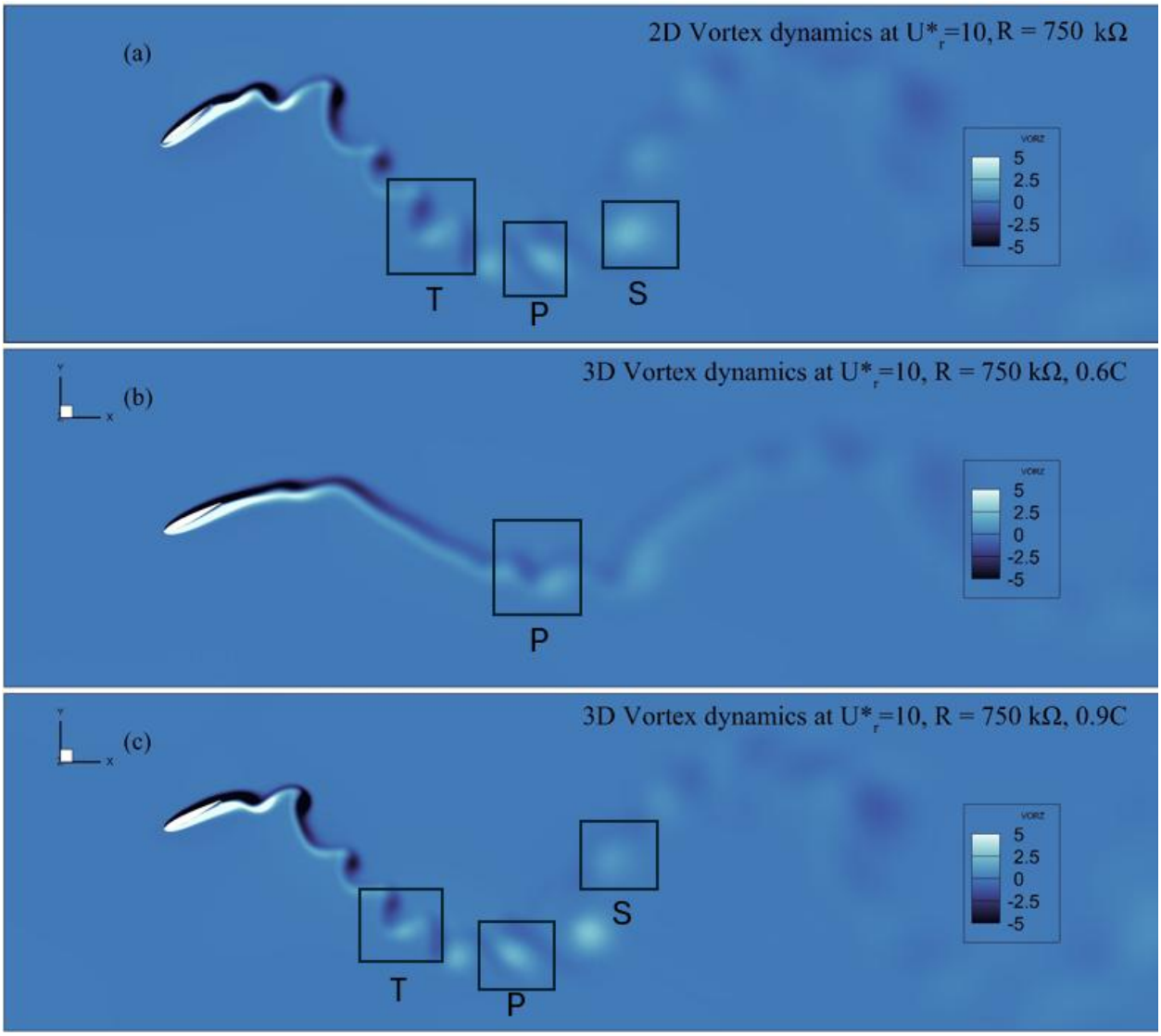

Figure 33: Comparison of 2D vortex dynamics at U_r^* =10 and 3d vortex dynamics at different spanwise length and R = 750 $k\Omega$

- **Voltage output**

From the 3D simulation results, the non-dimensional RMS voltage output was calculated for different spanwise lengths at U_r^* = 10. It is evident that the smallest span (0.3c) produces very low voltage output, while span of 0.6c shows an increased output, and 0.9c achieves the

highest voltage. When comparing the 3D results with the 2D case, the 0.9c 3D output is closest to the 2D results across most load resistances. However, at $\mathrm{R} = 750\ \mathrm{k}\Omega$, the 3D simulations exhibit a higher voltage output than the corresponding 2D results, indicating the influence of spanwise effects on energy harvesting.

Table 8: Non-dimensional 3D and 2D voltage output at different 'R' and spanwise length

	L = Spanwise length	**R = 250 kΩ**	**R = 500 kΩ**	**R =750 kΩ**
2D	infinite	**0.4921**	**0.8888**	**0.9156**
3D	0.3c	0.0080	0.0039	0.0010
3D	0.6c	0.5179	0.6779	0.3009
3D	0.9c	**0.5209**	**0.9074**	**0.9645**

Conclusions

This study investigates the nonlinear aeroelastic dynamics and energy harvesting performance of a two-degrees-of-freedom NACA 0012 airfoil under varying reduced velocities and electrical resistances. For the 2D simulations, the system exhibits complex responses driven by strong fluid-structure interactions, including quasi-nonlinear, periodic nonlinear, and chaotic behaviors. Oscillations begin near $U_r^* = 6$, with large-amplitude limit cycle oscillations appearing around $U_r^* = 8$ in the absence of electrical loading. Increasing electrical resistance shifts the onset of nonlinearity to higher reduced velocities due to added load-induced damping. FFT analysis reveals both odd and even harmonics, indicating energy content, which gradually diminishes with higher resistive loads. Phase portraits and Poincaré maps capture transitions between different dynamic states, showing that reduced velocity and resistance govern the nonlinear characteristics. Voltage output follows the lift coefficient trends, peaking at an optimal resistance, beyond which it saturates or declines due to suppressed nonlinearities. Vortex shedding patterns, including single (S), paired (P), triplet (T), multiple pair (mP), and P+S (in chaotic states), correlate with bifurcations and reduce as damping increases. Overall, the 2D results demonstrate that nonlinearity enhances energy harvesting but only within specific ranges of reduced velocity and load resistance.

For the 3D simulations, spanwise lengths of 0.3c, 0.6c, and 0.9c are considered to investigate the influence of spanwise effects on system dynamics and energy harvesting. At 0.3c of span, the system is predominantly damped with very low oscillation amplitudes, exhibiting linear behavior across all resistances. For 0.6c, nonlinear behavior emerges up to $R = 500\ k\Omega$,

but higher resistance at $\mathrm{R} = 750\ \mathrm{k}\Omega$, reduces the nonlinearity and associated vortex activity. At 0.9c, however, nonlinear dynamics persist across all resistances, with multiple-pattern vortex shedding (S, P, T, mP) clearly observed. The 3D results for the 0.9c span show close agreement with the 2D configuration in terms of vortex shedding sequences, phase portraits, Poincare maps, and FFT spectra, indicating that larger span length shows stronger nonlinear interactions across different load resistances. Voltage output is higher by 0.9c span compared to smaller span lengths, particularly at higher resistances, demonstrating the positive influence of spanwise extent on energy harvesting performance.

In summary, the study highlights how reduced velocity, electrical resistance, and spanwise length control the onset, amplitude, and nature of nonlinearity and vortex dynamics. While 2D simulations capture the general trends and mechanisms, 3D simulations reveal that spanwise effects are critical for sustaining nonlinearity coming from the fluid part and maximizing energy harvesting. These findings provide guidelines for parameter selection in experimental setups and the design of practical flutter-based energy harvesters.

Future Recommendations

The following directions are recommended for future research based on this study:

- Future studies should explore tandem or multiple-foil configurations to assess how wake interactions influence both individual and collective energy harvesting performance. *
- Investigating the effects of structural nonlinearities, including geometric and material nonlinearities, alongside fluid-induced nonlinearities could provide insight into how dual sources of nonlinearity affect oscillation amplitudes, vortex dynamics, and voltage generation, and overall energy harvesting.
- Extending the analysis to high-speed flows with flexible structures would allow evaluation of realistic aerodynamic or hydrodynamic conditions, helping to optimize energy harvesting for practical applications such as flutter-based devices, UAVs, or tidal energy systems.

Bibliography

[1] M. Bryant and E. Garcia, “Development of an aeroelastic vibration power harvester,” in *Active and Passive Smart Structures and Integrated Systems 2009*, 2009, pp. 409–418.

[2] A. Abdelkefi, A. H. Nayfeh, and M. R. Hajj, “Design of piezoaeroelastic energy harvesters,” *Nonlinear Dyn*, vol. 68, pp. 519–530, 2012.

[3] Q. Zhu, “Optimal frequency for flow energy harvesting of a flapping foil,” *J Fluid Mech*, vol. 675, pp. 495–517, 2011.

[4] Y. Xia, S. Michelin, and O. Doaré, “Resonance-induced enhancement of the energy harvesting performance of piezoelectric flags,” *Appl Phys Lett*, vol. 107, no. 26, 2015.

[5] M. Boudreau, M. Picard-Deland, and G. Dumas, “A parametric study and optimization of the fully-passive flapping-foil turbine at high Reynolds number,” *Renew Energy*, vol. 146, pp. 1958–1975, 2020.

[6] T. Villeneuve, M. Boudreau, and G. Dumas, “Assessing the performance and the wake recovery rate of flapping-foil turbines with end-plates and detached end-plates,” *Renew Energy*, vol. 179, pp. 206–222, 2021.

[7] T. Kinsey and G. Dumas, “Parametric study of an oscillating airfoil in a power-extraction regime,” *AIAA journal*, vol. 46, no. 6, pp. 1318–1330, 2008.

[8] M. F. Daqaq *et al.*, “Micropower generation using cross-flow instabilities: a review of the literature and its implications,” *J Vib Acoust*, vol. 141, no. 3, p. 30801, 2019.

[9] K. Shoele and R. Mittal, “Energy harvesting by flow-induced flutter in a simple model of an inverted piezoelectric flag,” *J Fluid Mech*, vol. 790, pp. 582–606, 2016.

[10] S. Orrego *et al.*, “Harvesting ambient wind energy with an inverted piezoelectric flag,” *Appl Energy*, vol. 194, pp. 212–222, 2017, doi: https://doi.org/10.1016/j.apenergy.2017.03.016.

[11] M.-J. Chern, T.-Y. Chou, D. G. Tewolde, and F. D. Suprianto, “Fully Passive Energy Harvesting from Heaving and Pitching Airfoils: Oscillation Response Patterns and Vortex Dynamics in Fluid Flow,” *J Fluids Struct*, vol. 133, p. 104255, 2025.

[12] X. Shan, H. Tian, H. Cao, J. Feng, and T. Xie, “Experimental investigation on a novel airfoil-based piezoelectric energy harvester for aeroelastic vibration,” *Micromachines (Basel)*, vol. 11, no. 8, p. 725, 2020.

[13] H. Farooq, M. S. U. Khalid, I. Akhtar, and A. Hemmati, “Nonlinear response of passively flapping foils,” *Ocean Engineering*, vol. 261, p. 112071, 2022.

[14] Z. Wang, L. Du, J. Zhao, and X. Sun, “Structural response and energy extraction of a fully passive flapping foil,” *J Fluids Struct*, vol. 72, pp. 96–113, 2017.

[15] D. T. Akcabay and Y. L. Young, “Hydroelastic response and energy harvesting potential of flexible piezoelectric beams in viscous flow,” *Physics of Fluids*, vol. 24, no. 5, 2012.

[16] A. Mehmood, A. Abdelkefi, M. R. Hajj, A. H. Nayfeh, I. Akhtar, and A. O. Nuhait, “Piezoelectric energy harvesting from vortex-induced vibrations of circular cylinder,” *J Sound Vib*, vol. 332, no. 19, pp. 4656–4667, 2013, doi: https://doi.org/10.1016/j.jsv.2013.03.033.

[17] A. Abdelkefi, M. Ghommem, A. O. Nuhait, and M. R. Hajj, “Nonlinear analysis and enhancement of wing-based piezoaeroelastic energy harvesters,” *J Sound Vib*, vol. 333, no. 1, pp. 166–177, 2014.

[18] S. Mazharmanesh, J. Young, F.-B. Tian, S. Ravi, and J. C. S. Lai, “Energy harvesting of inverted piezoelectric flags in an oscillating flow,” *J Fluids Struct*, vol. 115, p. 103762, 2022.

[19] “citations-20250821T205108”.

[20] R. Hagihghi, A. Razmjou, Y. Orooji, M. E. Warkiani, and M. Asadnia, “A miniaturized piezoresistive flow sensor for real-time monitoring of intravenous infusion,” *J Biomed Mater Res B Appl Biomater*, vol. 108, no. 2, pp. 568–576, 2020.

[21] D. P. Arnold, “Review of microscale magnetic power generation,” *IEEE Trans Magn*, vol. 43, no. 11, pp. 3940–3951, 2007.

[22] D. J. Inman and B. L. Grisso, “Towards autonomous sensing,” in *Smart Structures and Materials 2006: Sensors and Smart Structures Technologies for Civil, Mechanical, and Aerospace Systems*, 2006, pp. 248–254.

[23] C. De Marqui Jr and A. Erturk, “Electroaeroelastic analysis of airfoil-based wind energy harvesting using piezoelectric transduction and electromagnetic induction,” *J Intell Mater Syst Struct*, vol. 24, no. 7, pp. 846–854, 2013.

[24] C. R. dos Santos, F. D. Marques, and M. R. Hajj, “The effects of structural and aerodynamic nonlinearities on the energy harvesting from airfoil stall-induced oscillations,” *Journal of Vibration and Control*, vol. 25, no. 14, pp. 1991–2007, 2019.

[25] A. Abdelkefi, R. Vasconcellos, A. H. Nayfeh, and M. R. Hajj, “An analytical and experimental investigation into limit-cycle oscillations of an aeroelastic system,” *Nonlinear Dyn*, vol. 71, pp. 159–173, 2013.

[26] A. H. Nayfeh and D. T. Mook, *Nonlinear oscillations*. John Wiley & Sons, 2024.

[27] E. H. Dowell and D. Tang, “Nonlinear aeroelasticity and unsteady aerodynamics,” *AIAA journal*, vol. 40, no. 9, pp. 1697–1707, 2002.

[28] S. Badrinath, C. Bose, and S. Sarkar, “Identifying the route to chaos in the flow past a flapping airfoil,” *European Journal of Mechanics-B/Fluids*, vol. 66, pp. 38–59, 2017.

[29] S. Mazharmanesh, J. Young, F.-B. Tian, S. Ravi, and J. C. S. Lai, “Coupling performance of two tandem and side-by-side inverted piezoelectric flags in an oscillating flow,” *J Fluids Struct*, vol. 119, p. 103874, 2023.

[30] H. Farooq, “Numerical simulation of micro power generation through fluid structure interaction,” Centre for Advanced Studies in Pure and Applied Mathematics (CASPAM), Bahauddin Zakariya University, Multan, Pakistan, 2022.

[31] A. De Boer, M. S. der Schoot, and H. Bijl, “Mesh deformation based on radial basis function interpolation,” *Comput Struct*, vol. 85, no. 11–14, pp. 784–795, 2007.

[32] T. C. S. Rendall and C. B. Allen, “Efficient mesh motion using radial basis functions with data reduction algorithms,” *J Comput Phys*, vol. 228, no. 17, pp. 6231–6249, 2009.

[33] F. M. Bos, B. W. van Oudheusden, and H. Bijl, “Radial basis function based mesh deformation applied to simulation of flow around flapping wings,” *Comput Fluids*, vol. 79, pp. 167–177, 2013.

[34] B. P. Leonard, “A stable and accurate convective modelling procedure based on quadratic upstream interpolation,” *Comput Methods Appl Mech Eng*, vol. 19, no. 1, pp. 59–98, 1979.

[35] H. Farooq, A. Ali, and I. Akhtar, “Numerical Simulation of Micro Power Generation through Fluid Structure Interaction”.

[36] H. Farooq, A. Saeed, I. Akhtar, and Z. Bangash, “Neural network-based model reduction of hydrodynamics forces on an airfoil,” *Fluids*, vol. 6, no. 9, p. 332, 2021.

[37] H. Farooq, M. Ghommem, M. S. U. Khalid, and I. Akhtar, “Numerical investigation of hydrodynamic performance of flapping foils for energy harvesting,” *Ocean Engineering*, vol. 260, p. 112005, 2022.

[38] E. H. Dowell, *A modern course in aeroelasticity*, vol. 264. Springer Nature, 2021.

[39] A. Mehmood, A. Abdelkefi, M. R. Hajj, A. H. Nayfeh, I. Akhtar, and A. O. Nuhait, “Piezoelectric energy harvesting from vortex-induced vibrations of circular cylinder,” *J Sound Vib*, vol. 332, no. 19, pp. 4656–4667, 2013.

[40] H. Farooq, M. S. U. Khalid, I. Akhtar, and A. Hemmati, “Comparative performance of nonlinear energy harvesters through strongly coupled fluid-structure-electrical interactive models,” *J Fluids Struct*, vol. 121, p. 103957, 2023, doi: https://doi.org/10.1016/j.jfluidstructs.2023.103957.

[41] O. A. Marzouk and A. H. Nayfeh, “Characterization of the flow over a cylinder moving harmonically in the cross-flow direction,” *Int J Non Linear Mech*, vol. 45, no. 8, pp. 821–833, 2010.

[42] M. S. U. Khalid and I. Akhtar, “Characteristics of flow past a symmetric airfoil at low Reynolds number: a nonlinear perspective,” in *ASME International Mechanical Engineering Congress and Exposition*, 2012, pp. 167–175.